New Journal of Physics
An Institute of Physics and Deutsche Physikalische Gesellschaft Journal

The nonlinear drift wave instability and its role in tokamak edge turbulence

Bruce D Scott
Max-Planck-Institut für Plasmaphysik, EURATOM Association,
Boltzmannstrasse 2, D-85748 Garching, Germany
E-mail: bds@ipp.mpg.de

New Journal of Physics **4** (2002) 52.1–52.30 (http://www.njp.org/)
Received 8 February 2002, in final form 9 April 2002
Published 22 July 2002

Abstract. Drift wave turbulence, in general a balance between $\boldsymbol{E} \times \boldsymbol{B}$ drift turbulence in planes perpendicular to, and dissipative wave dynamics parallel to, a background magnetic field, is a hallmark example of nonlinearity in plasma physics. The turbulence generally has the same basic character in a sheared magnetic field lying in closed surfaces whether linear instabilities are present or not. Only when the linear forcing terms are dominant does this situation not prevail; it is not analogous to neutral fluid turbulence where pure linear forcing is balanced by pure nonlinear mixing and decorrelation. Detailed computations show that two types of nonlinearity are simultaneously present: advection of fluid vorticity by the $\boldsymbol{E} \times \boldsymbol{B}$ flows, which tends to have a scattering character, and $\boldsymbol{E} \times \boldsymbol{B}$ advection of pressure disturbances, which has the familiar diffusive mixing character. The vorticity nonlinearity excites the turbulence, acting against the mostly linear parallel dynamics which constrains it, while the pressure nonlinearity provides dissipation via transfer to ever smaller scales. The practical result is that the saturated level of the turbulence and the resulting averaged thermal energy transport are controlled principally by these nonlinear mechanisms even when moderate linear instabilities are present. The model is mostly applicable to tokamak edge turbulence, for which the linear forcing effects are sufficiently moderate that the nonlinear physics is allowed to operate.

1. Introduction—drift wave dynamics and the nonlinear instability

Drift waves are a class of small amplitude, low frequency eigenmodes [1] which exist in a low beta plasma in a background magnetic field ($\boldsymbol{B}$) with a pressure gradient (∇p). An MHD equilibrium is assumed, with $\nabla p \perp \boldsymbol{B}$. Low beta means the gas pressure is small compared to the magnetic field energy density and low frequency means sufficiently slow dynamics that

1367-2630/02/000052+30$30.00

the background magnetic field is dynamically incompressible. In practical terms this means responses which are slower than compressional Alfvén waves propagating perpendicular to the magnetic field and the gyrofrequency motion of any particle species. The plasma is assumed to be fully ionized and, in the basic models, to have one singly charged ion species with equal ion and electron densities. The basic character of the dynamics is a turbulent, multi-scale distribution of $\boldsymbol{E} \times \boldsymbol{B}$ velocity disturbance which advects the background gradient in drift planes (locally perpendicular to $\boldsymbol{B}$) to cause pressure disturbances of similar time and space scales, with the two disturbances coupled together by self-consistent currents parallel to $\boldsymbol{B}$ [2]. In general, the dynamics of the currents is electromagnetic [3], especially in three-dimensional (3D) turbulence [4]. The state variables are the electrostatic potential (ϕ, the stream function for the $\boldsymbol{E} \times \boldsymbol{B}$ velocity given by $\boldsymbol{v}_E = [c/B^2]\boldsymbol{B} \times \nabla\phi$) and the electron pressure (p_e), and the flux variables are the parallel electric current density ($J_\parallel$) and parallel ion velocity ($u_\parallel$); together, these four comprise the list of dependent variables in the simplest self-consistent model of drift wave dynamics. For greater realism the temperatures can be added but the qualitative nature of the dynamics does not change [5]. Both state variables act as force potentials for $J_\parallel$ in the electron equation of motion parallel to the magnetic field, and the compression of $J_\parallel$ along the magnetic field reinforces both ϕ and p_e. This set of parallel coupling mechanisms among $\tilde{\phi} \leftrightarrow \tilde{J}_\parallel \leftrightarrow \tilde{p}_e$ in the disturbances is also called the adiabatic response; it is what holds the drift wave dynamical system together (the tilde always refers to disturbed quantities; in most basic models only p_e among the dependent variables is nonzero in the background).

The free energy source for drift wave turbulence is the background pressure gradient. Direct dissipation is principally either resistive friction or electron Landau damping, acting on the parallel electron dynamics and hence making the coupling dissipative. In the simplest models the resistive friction is assumed to be sufficient that fluid equations for both electrons and ions can model the various processes involved. Dissipation in the ion parallel dynamics (sound waves) can lead to further losses. The dynamics in a realistic turbulent setting is fundamentally nonlinear and significantly different from the basic linear eigenmodes that were first studied; hence the distinction between drift waves and drift wave turbulence [2, 6]–[8]. In turbulence, the drive is self-consistently determined, and a turbulent cascade of the pressure disturbances to arbitrarily small scales becomes an important route to dissipation [5], as will be shown more fully herein.

Typical time and space scales in laboratory plasmas for this type of dynamics are about 10 μs and 1 cm (perpendicular) and several metres (parallel to $\boldsymbol{B}$), as observations using several diagnostics in the edge regions of tokamaks and stellarators indicate [9]–[16]. It is particularly important where the background gradient scale length and the parallel system size satisfy $L_\perp \ll L_\parallel$, so that the wavenumber components of the disturbances can satisfy $k_\parallel \ll k_\perp$. In plasmas in the edge regions of fusion experiments all these conditions are well satisfied, and additionally the details of the geometry of closed, nested magnetic flux surfaces lead to the feature that, for finite sized disturbances (localized but of finite extent in the plane perpendicular to $\boldsymbol{B}$), the parallel gradient cannot vanish on average [17]. This ensures importance for the adiabatic response, which is supported by the indication that, where data for $\tilde{\phi}$ are available, one finds the two state variables with similar statistics and at similar amplitude levels, and with an inferred transport level which can account for the thermal transport indicated by power balance studies [9]. A central role is thereby suggested for drift wave dynamics in the turbulence observed in these edge plasmas [2, 7]. The most important application of this model at the present time is to describe this edge turbulence, possibly also extending to the more interesting

confinement phenomena [18].

A key consideration in drift wave turbulence is nonlinear instability [19], also referred to as self-sustained turbulence [7]. Simple drift waves are known to be linearly stable or at least very weak [20], hence their lack of general favour in discussions of turbulent transport in tokamak plasmas [21]. Drift waves are so named because they drift in the electron diamagnetic drift direction given by $\nabla p \times \boldsymbol{B}$; that is, within the magnetic flux surface but perpendicular to $\boldsymbol{B}$. In order to cause a net thermal transport whose direction is radially outward (down the gradient), there must be a phase shift of $\tilde{p}_e$ ahead of $\tilde{\phi}$ in this drift direction [22]. The nature of the linear eigenmodes in a sheared magnetic field is very delicate, so much so that a small nonlinear diffusive effect on the electrons only is sufficient to cause destabilization [19]. In fully developed turbulence the changes to the mode structure are overwhelming, with the result that nonlinear advection by the $\boldsymbol{E} \times \boldsymbol{B}$ turbulence is able to cause robust nonlinear instability—since the turbulence is responsible for its own free energy access, this process is called self-sustained turbulence [7]. This drift wave turbulence is, in general, robust enough to account for the basic properties observed in tokamak edge fluctuations [23].

The tokamak does not have the geometry of a sheared slab, however; the magnetic field lines are curved and the field strength has a gradient. These two effects work together in a toroidal field, as both the magnetic curvature and gradient vectors are approximately equal to $\boldsymbol{r} = -\nabla R/R$, where R is the major radius position. When this lines up with ∇p, two-dimensional (2D) instabilities called interchange modes, occur [24], very similar to the Rayleigh–Taylor instabilities of fluid dynamics [25]. In a toroidal magnetic field, the sign of $\boldsymbol{r} \cdot \nabla p$ changes sinusoidally as one follows the field line; on the inboard (towards $R = 0$) side of the flux surface $\boldsymbol{r} \cdot \nabla p < 0$ and on the outboard side $\boldsymbol{r} \cdot \nabla p > 0$. This gives rise to the ballooning effect, by which the instability balloons to the outboard side [26, 27]. Like interchange modes, these are fundamentally MHD modes, whose qualitative nature is the same in one-fluid and two-fluid models. In general, turbulence in a toroidal setting has both the ballooning and drift wave mechanisms at its disposal. A description of tokamak or stellarator edge turbulence must face the possibilities of both mechanisms, and do so in the context of fully developed turbulence. We already know that drift wave turbulence is very different from drift waves; it follows that such edge turbulence cannot be assessed using the properties of linear eigenmodes and instabilities. Diagnostics which treat the underlying physics as well as the statistical morphology of the turbulence in a general 3D computation have found an important use [4, 5, 28]. Herein, they are used to directly compare the situation in $\boldsymbol{E} \times \boldsymbol{B}$ turbulence in a sheared magnetic field in toroidal geometry, reflecting tokamak flux surfaces, to cases run at the same parameters but with slab geometry (neglecting the toroidal effects) and with a resistive MHD model (neglecting the $\tilde{J}_{\|} \leftrightarrow \tilde{p}_e$ coupling mechanism). The mode structure found for the general case more closely resembles the pure drift wave control case, and it differs drastically from what one finds using the resistive MHD model. The additional complications of temperature effects in both electrons and ions are briefly introduced, enough to show that this situation persists for typical parameters and magnetic geometry for tokamak edge turbulence. Self-sustained turbulence representing the drift wave nonlinear instability is therefore very relevant to edge turbulence, and it is important to note that neither linear instability nor standard MHD conventions are applicable to treat the situation. The reasons are that drift wave dynamics does not exist in MHD, turbulence is a statistical phenomenon not treatable using coherent eigenmodes or even nonlinear structures, and the $\boldsymbol{E} \times \boldsymbol{B}$ advective nonlinearities are crucial to establishing the dynamical character in the first place.

2. The four-field DALF3 model

The simplest 3D model of drift wave dynamics, which takes the self-consistent adiabatic response into account and allows it an electromagnetic character, is a four-field model in toroidal flux tube geometry called DALF3 (the local drift Alfvén model [4] but omitting the temperature dynamics). The state variables are the electrostatic potential $\tilde{\phi}$ and the electron pressure $\tilde{p}_e$, and the flux variables are the parallel current $\tilde{J}_\parallel$ and the parallel ion velocity $\tilde{u}_\parallel$. In Ohm's law, electromagnetic induction, electron inertia and resistive friction are all retained. The adiabatic response is the reaction of the parallel current, controlled by those three effects, to the pressure/potential static force imbalance, acting to couple $\tilde{p}_e$ and $\tilde{\phi}$ through the shear Alfvén dynamics. We allow for a finite background ion temperature in general, with $\tau_i = T_i/T_e$, but note that, since $\tilde{p}_i = \tau_i \tilde{p}_e$, there is no additional equation. The model equations in simplified sheared flux tube geometry are [4, 29]

$$\frac{1}{B^2}\left[\frac{\mathrm{d}}{\mathrm{d}t}\nabla_\perp^2(\tilde{\phi}+\tilde{p}_i)+(\nabla \boldsymbol{v}_E):(\nabla\nabla\tilde{p}_i)\right] = B\nabla_\parallel\frac{\tilde{J}_\parallel}{B} - \mathcal{K}(\tilde{p}_e+\tilde{p}_i) \tag{1}$$

$$\hat{\beta}\frac{\partial \tilde{A}_\parallel}{\partial t} + \hat{\mu}\frac{\mathrm{d}\tilde{J}_\parallel}{\mathrm{d}t} + C\tilde{J}_\parallel = \nabla_\parallel(p_e+\tilde{p}_e-\tilde{\phi}) \tag{2}$$

$$\frac{\mathrm{d}}{\mathrm{d}t}(p_e+\tilde{p}_e) = B\nabla_\parallel\frac{\tilde{J}_\parallel-\tilde{u}_\parallel}{B} - \mathcal{K}(\tilde{p}_e-\tilde{\phi}) \tag{3}$$

$$\hat{\epsilon}\frac{\mathrm{d}\tilde{u}_\parallel}{\mathrm{d}t} = -\nabla_\parallel(p_e+p_i+\tilde{p}_e+\tilde{p}_i) \tag{4}$$

with Ampère's law $\tilde{J}_\parallel = -\nabla_\perp^2\tilde{A}_\parallel$ and background gradient $p_e = -\omega_p x$, with ω_p a parameter and $p_i = \tau_i p_e$. The extra term on the left side of equation (1) results from the lowest-order gyroviscosity cancellation [30], which is required to conserve free energy properly among all the transfer effects involving $\nabla_\parallel$ and $\mathcal{K}$. The differential operators are the $\boldsymbol{E}\times\boldsymbol{B}$ advection $\mathrm{d}/\mathrm{d}t = \partial/\partial t + v_E^\mu\nabla_\mu$, the perpendicular Laplacian $\nabla_\perp^2 = g^{-1/2}\nabla_\mu g^{1/2} g_\perp^{\mu\nu}\nabla_\nu$, the parallel gradient $\nabla_\parallel = b^\mu\nabla_\mu$ and the magnetic curvature operator $\mathcal{K} = \mathcal{K}^\mu\nabla_\mu$, where $v_E^x = -\nabla_y\tilde{\phi}$ and $v_E^y = \nabla_x\tilde{\phi}$ with $v_E^s = 0$ give the $\boldsymbol{E}\times\boldsymbol{B}$ velocity, and $b^x = \hat{\beta}\nabla_y\tilde{A}_\parallel$ and $b^y = -\hat{\beta}\nabla_x\tilde{A}_\parallel$ give the disturbances in the magnetic field, with b^s describing part of the equilibrium. The flux tube geometry used is detailed elsewhere [31], as is the importance of global consistency which controls field line connection [17] (cf also section 5 below). The geometry is quantified by the perpendicular metric $g_\perp^{\mu\nu}$, the Jacobian $g = \det\{g_{\mu\nu}\}$, the background magnetic field strength B and unit vector projection b^s, and the curvature vector $\mathcal{K}^\mu$. For a torus (r,θ,φ) with field line pitch $q(r) = B^\varphi/B^\theta$, the simplified shifted metric flux tube model is given by

$$g^{xx} = 1 \qquad g_k^{xy} = \hat{s}(s-s_k) \qquad g = 1 \qquad g_k^{yy} = [1-(g_k^{xy})^2]/g^{xx} \tag{5}$$

$$B = b^s = 1 \tag{6}$$

$$\mathcal{K}^x = \omega_B\sin s \qquad \mathcal{K}_k^y = \omega_B[\cos s + \hat{s}(s-s_k)\sin s] \tag{7}$$

with s_k a global constant. The subscript k denotes the use of a different y coordinate system, chosen to set $g_k^{xy} = 0$ at each location $s = s_k$, where perpendicular derivatives are used. This yields an orthogonal representation on local drift planes at $s = s_k$ and incurs x-dependent shifts in the y coordinate:

$$y_k = y - \alpha_k(x) \qquad \alpha_k = \hat{s}s_k x \tag{8}$$

while taking s derivatives (with node spacing h_s):

$$2h_s \frac{\partial f}{\partial s}(x, y_k - \alpha_k, s_k) = f(x, y_{k+1} - \alpha_{k+1}, s_{k+1}) - f(x, y_{k-1} - \alpha_{k-1}, s_{k-1}) \tag{9}$$

mediated by the magnetic shear, which in this model is a constant parameter given by $\hat{s} = \mathrm{d}\log q/\mathrm{d}\log r$ at the local minor radius. (It is important to note that these shifts, dependent only upon x, do not merely reverse the field aligning in the coordinates, which involves redefining of y in terms of both s and x; cf [31].)

The normalization in terms of the drift scale $\rho_s = c_s/\Omega_i$ and frequency $c_s/L_\perp$ is standard, where $c_s^2 = T_e/M_i$ and $\Omega_i = eB/M_i c$ and $L_\perp$ is the background scale length for p_e (note that if $\omega_p = 1$, then $L_\perp$ is L_p). The parameters controlling the adiabatic response are

$$\hat{\beta} = \left(\frac{c_s/L_\perp}{v_A/qR}\right)^2 \qquad \hat{\mu} = \left(\frac{c_s/L_\perp}{V_e/qR}\right)^2 \qquad C = \frac{0.51\nu_e}{c_s/L_\perp}\hat{\mu} \tag{10}$$

where V_e is the electron thermal velocity ($V_e^2 = T_e/m_e$), ν_e is the conventional collision frequency and the 0.51 comes from the parallel resistivity [32]. The sound waves are controlled by $\hat{\epsilon} = (c_s/L_\perp)^2(qR/c_s)^2$, i.e. just the square of the parallel/perp scale ratio. The interchange effects are controlled by $\omega_B = 2L_\perp/R$, which can be set independently (slab geometry is $\omega_B = 0$). Nominal parameters corresponding to a typical tokamak plasma edge are

$$\hat{\beta} = 1 \qquad \hat{\mu} = 5 \qquad C = 7.65 \qquad \omega_B = 0.05 \qquad \hat{\epsilon} = 18\,350 \qquad \hat{s} = 1 \tag{11}$$

with $\omega_p = 1$, roughly reflecting physical parameters:

$$\begin{aligned} &n_e = 3 \times 10^{13}\ \mathrm{cm}^{-3} \qquad T_e = 70\ \mathrm{eV} \qquad B = 2.5\ \mathrm{T} \\ &R = 165\ \mathrm{cm} \qquad L_\perp = 4.25\ \mathrm{cm} \qquad q = 3.5 \end{aligned} \tag{12}$$

and with $\tau_i = 1$ an equal background temperature ratio. Cold ion models are recovered by setting $\tau_i = 0$, which removes the gyroviscosity correction by eliminating the ion diamagnetic component of the vorticity $\nabla_\perp^2(\tilde{\phi} + \tilde{p}_i)$. This is most appropriate for comparison to MHD models, which assume that perpendicular flow is given by $\boldsymbol{v}_E$. The standard resistive MHD model is recovered by setting $\tau_i = 0$, removing $\nabla_\parallel(p_e + \tilde{p}_e)$ in equation (2) and removing the $\nabla_\parallel(\tilde{J}_\parallel/B)$ and $\mathcal{K}(\tilde{p}_e)$ terms in equation (3). The first two of those terms are a requisite part of the adiabatic response, which is therefore absent in all MHD models.

Computations are nominally set up on a grid of isotropic cells in the xy plane (drift plane) with an anisotropic domain which is longer in the y direction. Enough grid nodes are set up in the s direction to contain the parallel responses to the $\boldsymbol{E} \times \boldsymbol{B}$ turbulence in the xy plane. The xy domain is 1×4 times $20\pi\rho_s$ on 64×256 nodes, with 16 nodes in the s direction in one connection length, $2\pi qR$. In normalized units the node spacings are $h_x = h_y = 20\pi/64$ and $h_s = 2\pi/16$. The time step is set to 0.05, momentarily revised downward when the Courant limits set by the nonlinearities demand such. The time and space discretizations follow the slope-limited MUSCL scheme of Van Leer [33] and Colella [34], as outlined in [5] for equations qualitatively very similar to these. The initial state is a random phase field (cf [7]) for $\tilde{p}_e$ in the xy plane, with a random scaling factor between 0.9 and 1.1 for the s direction, with the y coordinate shifted to line the disturbances up with the field lines. The initial rms amplitude is nominally 3.0. The drift wave mode structure develops naturally through the initial adiabatic response and the strong nonlinear vorticity dynamics.

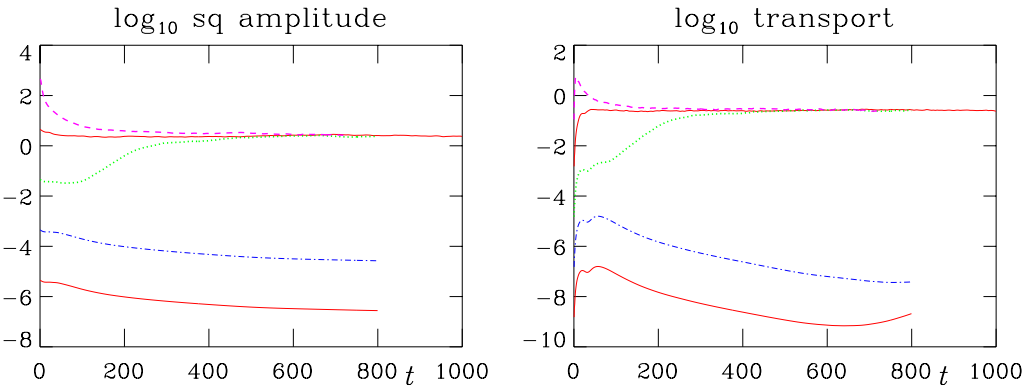

Figure 1. Squared amplitude and transport levels for initial states of various rms amplitudes given by A_0 values one order of magnitude apart, as given in the text. For small A_0 the disturbances decay, while beyond a threshold the nonlinear dynamics is strong enough for the turbulence to self-sustain.

3. Establishing the nonlinear instability

To establish the nonlinear instability one must find a situation where the linear damping mechanisms function properly for a reasonable grid resolution. Due to the combination of finite resolution and field line connection the linear system will always produce spurious grid modes after a finite time, even though these do not play a role in the turbulence due to the latter's finite correlation time (cf [4]). The onset of grid modes may be sufficiently delayed by choosing a very fine resolution in the x direction. We do this by increasing the x resolution by a factor of 4, leaving 256×256 grid nodes within an unchanged xy domain. For these cases the boundaries were periodic, set up as in appendix A of [31], and the magnetic shear was set to $\hat{s} = 1.2$, in keeping with the domain aspect ratio of 4 (further comments on the choice of boundary conditions are given in section 5, discussing the situation on closed, nested, toroidal flux surfaces). The parameters were $\tau_i = 0$, $C = 10$ and $\hat{\beta} = \hat{\mu} = 0.1$, setting up the cold-ion, collisional, electrostatic case, and $\hat{\epsilon} = 100$, small enough so that the sound waves stabilize the linear modes (these choices were also taken to put the situation close to that of the original 2D slab models described in [7]). The prototypical nonlinear instability is then shown using the same initial state, except for an overall scaling of $A_0 = 3 \times [10^{-3}, 10^{-2}, 10^{-1}, 10^{0}, 10^{1}]$, as shown in figure 1. The squared amplitude and transport are defined as $\langle \tilde{p}_e^2 \rangle / 2$ and $\langle \tilde{p}_e v_E^x \rangle$, respectively, averaged over each of the grid nodes.

Two things tell us that this is a nonlinear instability. First, the cases at very low amplitude find linear stability, since the nonlinearities are arbitrarily small. The general linear stability is underscored by the fact that all available degrees of freedom were initially excited, so that a serendipitous degree of symmetry is avoided. At finite initial amplitude, however, the nonlinear effects are present and the result is fully developed, statistically stationary turbulence. Second, there is a definite threshold in this initial amplitude level. If the disturbances are too small at $t = 0$, the nonlinearities are too small to affect the linear dynamics, and the disturbances decay. If the initial disturbances are strong enough, however, the turbulence sustains itself, with an eventual saturated amplitude independent of the initial one, provided the latter is over the threshold. The monotonicity of this result confirms that the nonlinearities are the cause of the instability and, at the same time, the mechanism by which the turbulence sustains itself.

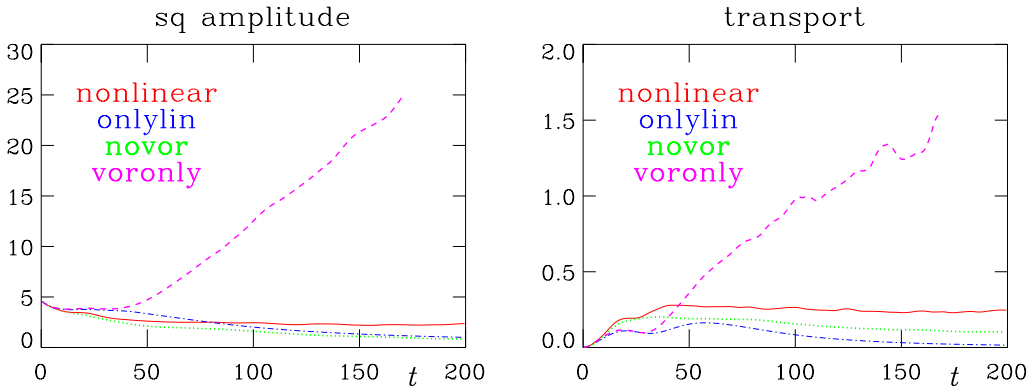

Figure 2. Squared amplitude and transport levels for a nonlinear initial rms amplitude $A_0 = 3$, with various nonlinearities shut off ('nonlinear' is with all nonlinearities, 'onlylin' is linear, 'voronly' is with $\boldsymbol{v}_E \cdot \nabla \nabla_\perp^2 \tilde{\phi}$ only, and 'novor' is with all nonlinearities except this one). The vorticity nonlinearity is the principal agent responsible for the self-sustained nature of the turbulence, and the other ones are required to provide saturation.

The question remains as to which one or which combination of nonlinearities is behind this self-sustained turbulence. In this case the only significant ones are $\boldsymbol{v}_E \cdot \nabla \nabla_\perp^2 \tilde{\phi}$ and $\boldsymbol{v}_E \cdot \nabla \tilde{p}_e$, the vorticity (sometimes called polarization [35]) and pressure (sometimes called $\boldsymbol{E} \times \boldsymbol{B}$ [30]) nonlinearities, respectively (simple measurement shows that the others are small by comparison). To diagnose this situation the case with $A_0 = 3$ and with all terms retained ('nonlinear') was re-run with no nonlinearities ('onlylin'), with the vorticity nonlinearity only ('voronly'), and then with all except the vorticity nonlinearity ('novor'). The results are shown in figure 2. Both of these cases in which the vorticity nonlinearity is absent produced decaying disturbances, while the case with all nonlinearities found saturation as in figure 1. The interesting finding is the 'voronly' case: monotonically rising and much larger amplitude and transport levels, and no saturation. The vorticity nonlinearity is therefore found to be necessary and sufficient to cause the nonlinear instability, and furthermore we have found that the other nonlinearities are required to provide saturation.

The corresponding gradient drive and grid dissipation rates for these four cases are shown in figure 3. The gradient drive is the average flux divided by twice the total free energy so as to be expressed in terms of a growth rate [7]. The free energy is essentially fluctuation activity; it is defined at the beginning of section 4. Grid dissipation follows from the tendency of the nonlinearities collectively to transfer free energy to sub-grid scales (those smaller than the grid resolution). In this case it is part of the numerical scheme [5, 33, 34]; for more conventional schemes the grid dissipation must be added manually in the form of viscosity or diffusion terms. In either case, cascade to sub-grid scales is a physical effect, not a numerical one, which must be treated one way or another. Linear grid dissipation is due to the parallel dynamics.

We find that the drive rates are much larger when the nonlinearities are present. Which combination of nonlinearities is present does not make a large difference in the drive rate; either nonlinearity can redistribute the free energy vigorously enough to lead to strong free energy access—one redistributes $\tilde{\phi}$ and the other $\tilde{p}_e$, either way producing a large available space for the

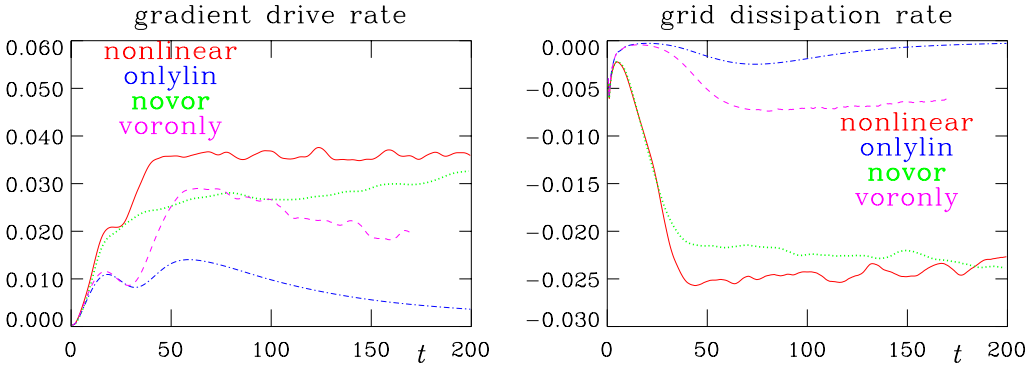

Figure 3. Gradient drive and grid dissipation rates for the four cases shown in figure 2. The pressure nonlinearity is the principal route to dissipation, while either nonlinearity can catalyze the free energy source. It is the absence of nonlinear transfer of free energy to sub-grid scales due to the missing pressure nonlinearity which leads to the continued growth of the case which retains only the vorticity nonlinearity.

mutual phase shift which is part of the average flux and hence the drive [7]. But the case with the vorticity nonlinearity by itself shows the smallest grid dissipation rate among the nonlinear cases even while leading to much larger free energy levels. This reveals the pressure nonlinearity as the principal saturation mechanism, in accordance with the results of figure 2. That the vorticity nonlinearity is required for self-sustainment is due to the detailed properties of the pressure nonlinearity: its cascade tendency results in its always causing more grid dissipation (plus the resistive dissipation, which is not shown) than drive. (Very similar results are obtained with more conventional numerical schemes which contain no grid dissipation directly in the $\boldsymbol{v}_E \cdot \nabla$ terms but which must insert it manually as noted above.) The information in figures 2 and 3 together thus show that the mechanism of self-sustainment in drift wave turbulence is increased gradient drive due to the nonlinearities, with the vorticity nonlinearity required to overcome the sub-grid dissipation in the pressure nonlinearity. The mechanism of saturation, in turn, is this transfer to sub-grid scales in the pressure nonlinearity.

4. Energy transfer analysis

Some insight as to the physical mechanism by which these $\boldsymbol{E} \times \boldsymbol{B}$ advection nonlinearities operate is gained by examining the free energy conservation theorem (sometimes this is called 'entropy') for the equations. We define the free energy density in terms of a set of quadratic quantities, one for each dependent variable, with coefficients chosen such that the parallel gradients and divergences are collectively conservative [6, 7]. The free energy density for the DALF3 model for $\tau_i = 0$ is given by

$$U = \frac{1}{2}\left(\frac{1}{B^2}|\nabla_\perp \tilde{\phi}|^2 + \tilde{p}_e^2 + \hat{\beta}|\nabla_\perp \tilde{A}_\parallel|^2 + \hat{\mu}\tilde{J}_\parallel^2 + \hat{\epsilon}\tilde{u}_\parallel^2\right). \tag{13}$$

Its rate of change is found by multiplying equations (1)–(4) by $-\tilde{\phi}$, $\tilde{J}_\parallel$, $\tilde{p}_e$ and $\tilde{u}_\parallel$, respectively, and manipulating some of the divergences implied in the $\nabla_\perp^2$ operator. The various energy

transfer channels become clear when the four parts are written separately:

$$\frac{1}{2}\frac{\partial}{\partial t}\frac{1}{B^2}|\nabla_\perp\tilde{\phi}|^2+\nabla\cdot()=\tilde{J}_\parallel\nabla_\parallel\tilde{\phi}-\tilde{p}_e\mathcal{K}(\tilde{\phi}) \tag{14}$$

$$\frac{1}{2}\frac{\partial}{\partial t}(\hat{\beta}|\nabla_\perp\tilde{A}_\parallel|^2+\hat{\mu}\tilde{J}_\parallel^2)+\nabla\cdot()=\tilde{J}_\parallel\nabla_\parallel\tilde{p}_e-\tilde{J}_\parallel\nabla_\parallel\tilde{\phi}-C\tilde{J}_\parallel^2 \tag{15}$$

$$\frac{1}{2}\frac{\partial}{\partial t}\tilde{p}_e^2+\nabla\cdot()=-\tilde{J}_\parallel\nabla_\parallel\tilde{p}_e+\tilde{u}_\parallel\nabla_\parallel\tilde{p}_e+\tilde{p}_e\mathcal{K}(\tilde{\phi})-\omega_p\tilde{p}_e\frac{\partial\tilde{\phi}}{\partial y} \tag{16}$$

$$\frac{1}{2}\frac{\partial}{\partial t}\hat{\epsilon}\tilde{u}_\parallel^2+\nabla\cdot()=-\tilde{u}_\parallel\nabla_\parallel\tilde{p}_e+\omega_p\hat{\beta}\tilde{u}_\parallel\frac{\partial\tilde{A}_\parallel}{\partial y} \tag{17}$$

in which the divergences left over after the transfer channels are established are collected into $\nabla\cdot()$, not explicitly written. These divergence terms are homogeneous fluxes, while every other term is either a source, a transfer channel or a sink. Transfer channels are found by identifying identical terms of opposite sign in two equations; the others are sources and sinks. The sources arise from the background gradient, ω_p, generally dependent on the phase shifts between the two quantities in the product (e.g. $\tilde{p}_e$ and $\tilde{\phi}$). The sink is resistivity, denoted by C. The other important sinks are present in the $\boldsymbol{v}_E\cdot\nabla$ terms, which allow for free energy to be cascaded out of the spectrum to the small-scale side (these terms are in the divergences in each equation). There is also the sound wave dynamics, denoted by $\tilde{u}_\parallel$, which provide a transfer channel between $\tilde{p}_e$ and $\tilde{u}_\parallel$.

The principal transfer channels are two: the adiabatic response, which transfers energy through $\tilde{J}_\parallel\nabla_\parallel\tilde{p}_e$ between $\tilde{p}_e$ and $\tilde{J}_\parallel$, and then through $\tilde{J}_\parallel\nabla_\parallel\tilde{\phi}$ between $\tilde{J}_\parallel$ and $\tilde{\phi}$. The second piece of this is the familiar shear Alfvén coupling, and the first piece is the adiabatic coupling (dynamic compression in $\tilde{J}_\parallel$, absent in an MHD model). Secondly, we have the interchange effect, which transfers free energy through $\tilde{p}_e\mathcal{K}(\tilde{\phi})$ directly between $\tilde{p}_e$ and $\tilde{\phi}$ (quasistatic compression in $\boldsymbol{v}_E$). In the slab model we have been looking at, only the adiabatic response can allow the free energy entering the dynamics through $\omega_p\tilde{p}_e v_E^x$ to be transferred to the $\boldsymbol{E}\times\boldsymbol{B}$ vortices themselves. In the electrostatic limit, however, these are linear terms and we have already seen that by themselves they do not lead to instability. The role of the nonlinearities is then an enhancement effect which can make the various source, transfer and sink terms stronger, thereby changing the mode structure of the disturbances so that the turbulence can self-sustain.

The key to this is the self-consistent dependence of the source itself on the robustness with which the free energy is redistributed by all the effects. If the nonlinearities are small, then the ability of the rest of the system to resist the adiabatic response is weak, and the dynamics tends towards the adiabatic state:

$$\nabla_\parallel(\tilde{J}_\parallel/B)\to 0\Longrightarrow\tilde{\phi}\to\tilde{p}_e\Longrightarrow\langle\tilde{p}_e v_E^x\rangle\to 0$$

where the angle brackets denote a statistical average which, in practical terms, includes integration over the y direction. If $\tilde{p}_e\propto\tilde{\phi}$, then the source is zero on average. The nonlinearities must therefore act by opposing $\nabla_\parallel(\tilde{J}_\parallel/B)$, and they can do this in either the vorticity (1) or pressure (3) equations. In figure 4, we show the mean sizes of the energy transfer effects present in the vorticity nonlinearity $\boldsymbol{v}_E\cdot\nabla\nabla_\perp^2\tilde{\phi}$ and the nonadiabaticity $B\nabla_\parallel(\tilde{J}_\parallel/B)$. These are found by Fourier decomposing these two terms in k_y, multiplying by the complex conjugate of the Fourier component of $\tilde{\phi}$ at the same k_y, and then averaging the absolute magnitude of the products over (x,s,t), over the time interval $40<t<200$. The cases are labelled as in figure 2, and since the 'novor' and 'onlylin' cases do not actually retain $\boldsymbol{v}_E\cdot\nabla\nabla_\perp^2\tilde{\phi}$, their blue curve is drawn

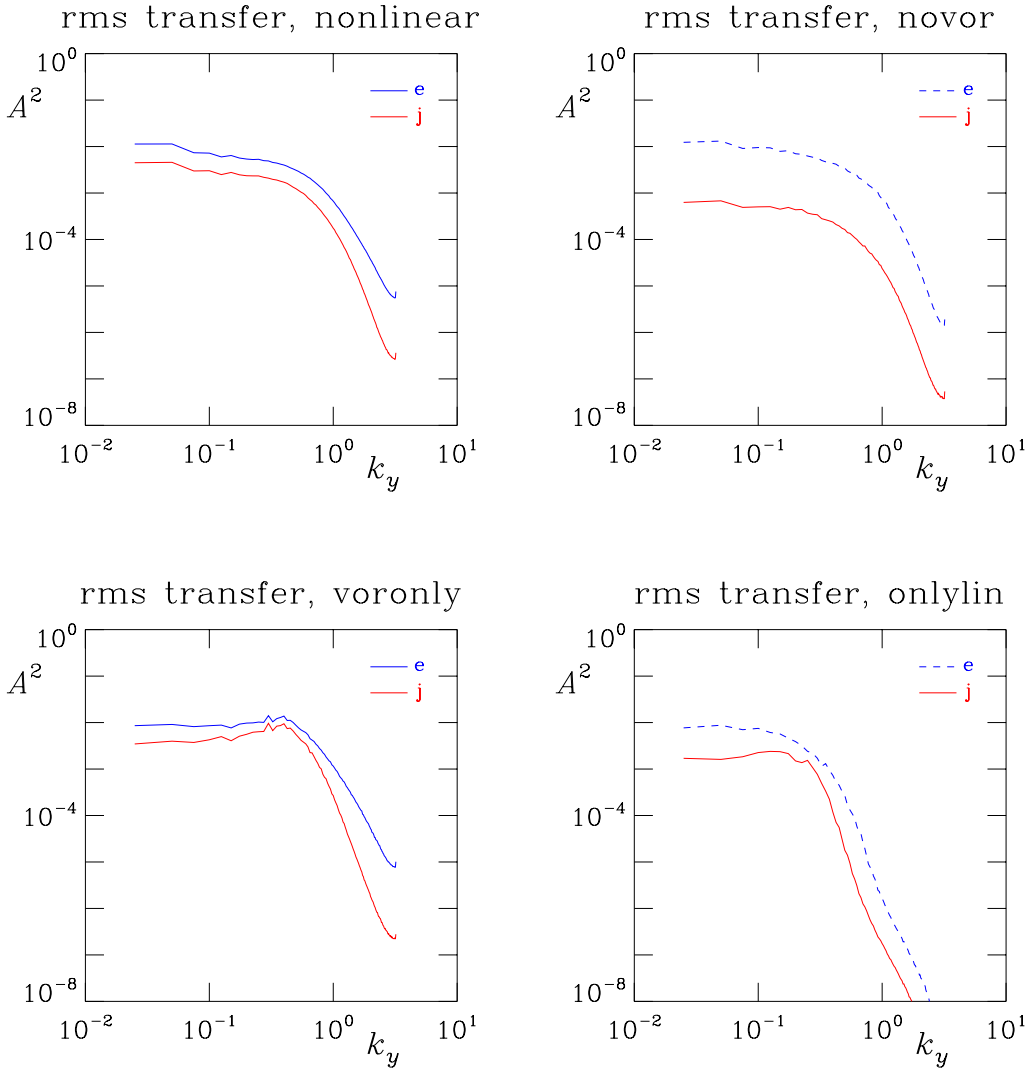

Figure 4. Rms energy transfer spectrum for the four cases shown in figures 2 and 3, normalized to the squared vorticity (enstrophy). The two cases in which $\boldsymbol{v}_E \cdot \nabla\nabla_\perp^2\tilde{\phi}$ is absent show the $\boldsymbol{E} \times \boldsymbol{B}$ transfer (blue, broken curve) at the level it would be if immediately switched on. The red curve shows the rms nonadiabaticity $\langle\tilde{\phi}B\nabla_\parallel(\tilde{J}_\parallel/B)\rangle$. Nonadiabatic dynamics is much stronger when $\boldsymbol{v}_E \cdot \nabla\nabla_\perp^2\tilde{\phi}$ is present; exciting this is the role of that nonlinearity. The smaller scales collapse if all nonlinearities are absent. Note that the 'voronly' case shows the vorticity nonlinearity to be most effective for about $0.3 < k_y < 1.0$.

broken to indicate how strong the nonlinear transfer into and out of the given k_y would be, were this term suddenly switched on. We find that the main effect of the pressure nonlinearity is to broaden the nonadiabaticity (red) curve, especially towards higher k_y. The main effect of the vorticity nonlinearity is to increase the nonadiabaticity, especially for medium k_y between about 0.3 and 1. The largest nonadiabaticity occurs where $\boldsymbol{v}_E \cdot \nabla\nabla_\perp^2\tilde{\phi}$ acts alone to peak it in this range. The shorter wavelengths at k_y larger than about 0.2 collapse entirely in the linear case. It

is interesting to note that in the 'novor' case the nonadiabaticity is very weak, but the vorticity transfer would be very strong if switched on. This reflects the chopped nature of $\tilde{\phi}$ when it is not scattered about by vorticity advection, and the fact that the $(\partial/\partial t)$ term in equation (1) causes very little nonadiabaticity by itself.

We have just found that $\boldsymbol{v}_E \cdot \nabla \nabla_\perp^2 \tilde{\phi}$ is necessary and sufficient for self-sustainment, it causes relatively little sub-grid dissipation and it is responsible for the robust nonadiabaticity one finds in the turbulence. So the mechanism must be a statistical balance between these two terms which does not involve too much dissipation. In addition, we found the dominant spectral range to be about $0.3 < k_y < 1.0$, indicating the important role for ρ_s scales to the overall dynamics, including the longer wavelengths. The vorticity dynamics in drift planes is basically that of a 2D Eulerian fluid, namely the cascade tendency is inverse, towards larger scales (this merely means a preference; the transfer to small scales is not zero) [36]. This property is responsible for the low level of grid dissipation we found when $\boldsymbol{v}_E \cdot \nabla \nabla_\perp^2 \tilde{\phi}$ was the only nonlinearity present. The higher levels we found in the cases with $\boldsymbol{v}_E \cdot \nabla \tilde{p}_e$ present result from its direct cascade tendency, which throws free energy out of the spectrum on the high-$k_\perp$ side and hence to sub-grid scales which are not involved in the dynamics. This is why the extra excitation one obtains from the vorticity nonlinearity, in a sense 'for free,' is required to recover self-sustainment, and why we found no saturation when the pressure nonlinearity was absent.

4.1. Physical mechanism of the nonlinear instability

The foregoing diagnosis is a necessary step before one could use the results concerning the amplitude and transport levels of the turbulence in constructing a physical picture of the nonlinear drift wave instability. The problem is too complicated for a first principles analytical calculation to simultaneously treat its two main features: statistical character and self-consistency. Turbulence is traditionally addressed in terms of a typical drive scale, a typical dissipation scale and an inertial energy cascade range in between. For fluid turbulence this is the direct cascade to viscous scales; for plasma turbulence this is the inverse cascade of the 2D $\boldsymbol{E} \times \boldsymbol{B}$ velocity field to larger scales [36], with the electron response assumed to be linear, providing instability, and with the ion response providing dissipation [37]. Both responses are either fluid (e.g. collisional, viscous dissipation in the parallel dynamics) or kinetic (e.g. Landau damping in the parallel dynamics). These pictures both contain assumptions which are found by the foregoing diagnosis to be inapplicable to drift wave turbulence: firstly, the response of the electrons is nonlinear except when it is so small as to be negligible; secondly, both cascade tendencies are simultaneously present, in different nonlinearities. The polarization ($\boldsymbol{E} \times \boldsymbol{B}$ vorticity) nonlinearity indeed has the 2D fluid inverse cascade tendency, since it conserves both energy and enstrophy but, at the same time, the pressure nonlinearity has the direct cascade tendency which results from having to conserve only the free energy. It is therefore not enough to speak of the energy cascade of the system as a whole (cf, e.g., [38]), because the two cascades are both active, each affecting only the free energy associated with its own dependent variable, in this case $\tilde{\phi}$ and $\tilde{p}_e$ [6]. Direct measurement of the associated energy transfer in the simple 2D drift wave models shows that, unless the electrons are unrealistically nearly adiabatic, the direct cascade tendency through $\tilde{p}_e$ is always the stronger [8]. The more customary models using the linear electron response with all the nonlinear dynamics in the ions are therefore ruled out, due to the fact that the electron response is so strongly nonlinear [6, 7]. Still less relevant is the older but still popular concept of adiabatic electrons with nonlinear ion dynamics providing all the

spectral transfer effects (cf, e.g., [39, 40]); these models are meant for turbulence in the hot core regions of magnetically confined plasmas, where it is expected that the passing electrons (those not trapped by the toroidal geometry) have no dynamical role. For dynamics at tokamak edge parameters this concept is entirely inapplicable.

In 3D, measurement of the energy transfer of enstrophy, $\boldsymbol{E} \times \boldsymbol{B}$ energy and thermal free energy (mean squared vorticity, $\boldsymbol{E} \times \boldsymbol{B}$ velocity, and pressure fluctuation amplitude, respectively) from modes $k_\perp \rho_s = 0.5$ to 0.3, from 0.4 to 0.2, and from 0.4 to 0.1 shows that the average of the transfers, giving the cascades, keeps these 2D properties (unsurprisingly, since the nonlinearity is itself 2D). However, we also find that in all cases, including the $\tilde{p}_e \leftrightarrow \tilde{J}_\parallel \leftrightarrow \tilde{\phi}$ transfer path which takes its character from the $\boldsymbol{v}_E \cdot \nabla \nabla_\perp^2 \tilde{\phi}$ nonlinearity which forces it, (1) the rms level of the energy transfer is much larger than the mean, and (2) the probability density function (PDF) of each transfer is dominantly Gaussian. This tells us that the function of the nonlinearities is not so much to give a cascade tendency, but to act statistically and to maintain the energy containing range of the spectrum as a unit. In turn, it tells us the type of model we have to build for the instability itself: not a low degree of freedom model, but a statistical one, and not one based upon the presence or absence of a particular cascade tendency. The cascades themselves play their role in the dissipation: that the vorticity cascade tendency is inverse, and that the sound wave activity is measured to be small (a consequence of the small size of $k_\parallel L_p$) tell us that the role of the vorticity nonlinearity is purely excitation, as we see from the fact that acting alone it causes relatively little dissipation. That the pressure cascade tendency is direct, that the parallel electron and ion dynamics are measured not to account for the overall dissipation at small scales, and that the measured dissipation is much greater when this nonlinearity is present tell us that the role of the pressure nonlinearity is diffusive mixing and therefore dissipation.

The basic physical picture of the nonlinear drift wave instability is therefore as follows:

(1) The vorticity nonlinearity broadens the PDF of the parallel current divergence $B\nabla_\parallel(\tilde{J}_\parallel/B)$.

(2) $\tilde{J}_\parallel$ is nonzero if $\tilde{h}_e = \tilde{p}_e - \tilde{\phi}$ is nonzero, because of the toroidal topology and magnetic shear.

(3) With larger $\tilde{J}_\parallel$ allowed, a larger range of phase shifts between $\tilde{p}_e$ and $\tilde{\phi}$ are allowed.

(4) With both positive and negative phase shifts statistically present, the side of the PDF with positive phase shifts is dynamically selected by the free energy source, ∇p_e.

(5) The source is ∇p_e, in the equation for $\tilde{p}_e$, the transfer path is $\tilde{p}_e \leftrightarrow \tilde{J}_\parallel \leftrightarrow \tilde{\phi}$ through the nonadiabatic $\nabla_\parallel$ terms, and the nonlinearities make the transfer path more robust than for linear waves, by broadening the PDF of the phase shifts for a given amplitude level.

(6) Most of the catalysis is done by the vorticity nonlinearity, because this one acts with a minimum of dissipation and it acts directly in the balance between the currents. The pressure nonlinearity has to act indirectly on the linear polarization current through its action on the partial time derivative $\partial \tilde{p}_e/\partial t$.

(7) The vorticity nonlinearity comes with little dissipation, making it necessary for overall excitation.

(8) Dissipation is done by the pressure nonlinearity, which is the saturation mechanism; dissipation through all channels of parallel dynamics is measured to be too small in 3D to account for the overall drive.

Magnetic shear and toroidal topology ('field line connection') is important in eliminating the degrees of freedom with $k_\parallel = 0$ but $k_\perp$ finite [17, 27]; these modes are otherwise dominant due to a small inverse cascade in $k_\parallel$ through the vorticity nonlinearity [41, 42]. Generally, field line connection is what guarantees the importance of the parallel dynamics, specifically the $\tilde{p}_e \leftrightarrow \tilde{J}_\parallel \leftrightarrow \tilde{\phi}$ transfer path, for any degree of freedom capable of free energy access ($k_y \neq 0$). The basic mechanism is the same in the sheared 2D and 3D slab models, because in 3D the x direction is essentially a free dimension; in the sheared 2D slab, finite extent in the x direction is how finite $k_\parallel$ is accessed. Statistically, however, the interaction between $\boldsymbol{v}_E \cdot \nabla$ and $k_\parallel$ is the same in both models, because $k_\parallel$ can self-consistently respond to $\boldsymbol{v}_E \cdot \nabla$ and only the average size of $k_\parallel$ is important.

Dissipation acts upon subgrid scales, in the sense of high Reynolds number turbulence: the effective dissipation coefficient in the (upwind) numerical scheme is resolution dependent, but when test cases are run with doubled resolution the energy-containing range of the spectrum is not affected. All that happens is that the dissipation range of the spectrum is extended to smaller scales. High Reynolds number in this context means that the perpendicular electron ($\rho_e^2\nu_e$) and ion ($\rho_i^2\nu_i$) dissipation coefficients are much too small to be effective at scales down to ρ_s (cf [7]; these numbers are about 10^{-3} and 10^{-2}, respectively, in normalized units at the nominal parameters). Higher-order upwind schemes are well suited to this situation [43, 44], because their dissipation is automatically tuned. More conventional centred differencing and pseudospectral schemes have to have the dissipation inserted by hand; because its effective diffusion coefficient has to be much larger than $\rho_e^2\nu_e$ or $\rho_i^2\nu_i$ it is just as artificial as in the case of grid-dependent methods, and because it must be homogeneously applied and because centred differencing is inherently unstable for hyperbolic equations (e.g. advection and wave systems) [45], these schemes must have ultimately more inherent dissipation at the same resolution than higher-order upwind schemes, even though they have less than first-order upwind schemes. Ultimately, the higher-order upwind schemes converge for fully developed turbulence at a lower resolution than do centred differencing schemes. In this context, it is important to note that spectral and pseudospectral schemes for the spatial derivatives have the same properties as do centred difference schemes of all orders, just with a different numerical growth rate for a given wave or advection problem [45]. It is also important to note that higher-order upwind schemes are very different from higher-order spatial differencing schemes; the entire space/time subsystem (e.g. all $\boldsymbol{v}_E \cdot \nabla$ terms, or all $\nabla_\parallel \tilde{J}_\parallel$ and $\nabla_\parallel \tilde{h}_e$ terms) is taken to higher order in both space and time together, and all dimensions of space and time work together in unsplit fashion [34].

5. The role of the nonlinear instability in tokamak edge turbulence

In practical terms in fusion research, the magnetic geometry includes the interchange effect to great importance. Practically every linear instability of interest has this as a central mechanism (cf, e.g., [46]). But in a real setting the fluctuations observed in $\tilde{\phi}$ and $\tilde{p}_e$ in tokamak and stellarator edge turbulence are found to be robustly nonlinear with a principally statistical character, and where both fluctuations are available they are found to have similar statistics and overall amplitude [9]–[16]. It is the regime of turbulence that is therefore relevant to turbulence and transport driven by gradients in magnetically confined plasmas. One cannot simply identify potentially dangerous linear instabilities and then arbitrarily conclude, even with a computation to hand, that the transport one finds is due to those same instabilities. One must compute and diagnose the dynamics in the proper context of turbulence before being in a position to classify

the dynamics one might find in a real situation. To do this in a straightforward way we revert to the model of section 2 with the nominal value of $\omega_B = 0.05$. This is basically a slab metric with the addition of the curvature operator, in what is often called a concentric circular, infinite aspect ratio tokamak model (the inverse aspect ratio is $\epsilon = a/R$, and finite ϵ introduces many complications, most of them of greater importance [28] than the usually considered Shafranov shift effect on the local magnetic shear [47]). The curvature vector introduces a direct energetic coupling between $\tilde{\phi}$ and $\tilde{p}_e$ which competes with the drift wave mechanism highlighted in sections 3 and 4. To understand the basic character of tokamak edge turbulence, together with the necessary effects and scales of motion a computation must carry in order to properly represent it, the competition between these two channels of free energy transfer from pressure gradient to $\boldsymbol{E} \times \boldsymbol{B}$ vortices must be decided in the context of fully developed turbulence in a realistic representation of the parametric and geometric situations in the tokamak edge.

Several alternative models for edge turbulence—all based upon linear instabilities—are mentioned here only in passing. Trapped electrons as a destabilizing mechanism [46] are generally not available to the large values of the typical ν_*, the ratio of the collisional de-trapping rate to the bounce time, whose standard definition is $\epsilon^{-3/2}\nu_e qR/V_e$. In normalized units we have $\nu_* = \epsilon^{-3/2}C\hat{\mu}^{-1/2}$, or about 40 for nominal parameters for $R/a = 3.3$. Radiation and ionization instabilities were considered [48] as an alternative to resistive ballooning before it was clearer that linear instabilities were not necessary to provide edge turbulence (cf [6, 7]). These are problematic even in principle because an additional growth or damping rate large enough to affect the self-sustained turbulence (generally about $0.1c_s/L_\perp$) would be catastrophic to the equilibrium, whose timescale even in the far edge is at least three orders of magnitude slower [49]. Investigation of this has shown that a level of flux surface averaged neutral density commensurate with maintenance of the equilibrium gave rise to negligible additional drive terms [50]. Other models have been even more inventive in searching for an external or kinetic effect which would yield a linear instability with the required properties. This is generally unnecessary, however, due to the delicate nature of linear instabilities in general and due to the fact that drift wave turbulence at edge parameters can function well enough without them. We do not further consider detailed kinetic effects beyond the need to retain Landau damping when the temperatures are considered (section 6), as an extension of parallel thermal conduction to weak but still finite collisionality [4]; other than this, the fluid model is perfectly adequate. Finite Larmor radius effects are moderate but not so important that their introduction strongly changes the physics [5]. It remains to consider the effects of toroidal curvature, as in this section, and then the effects of ion temperature, as in the next one. Linear instabilities can be superseded by the self-sustained drift wave turbulence even if they are relatively robust, as the mode structure of the turbulence is very resilient [51]. Herein, we consider drift wave, ballooning and ion temperature gradient (ITG) effects only within the context of fully developed turbulence; the detailed question of linear versus nonlinear mode structure is more of an academic issue, and which is addressed elsewhere ([52] for ballooning; a future one for the ITG). The present treatment should serve as a useful antidote to the still current but outdated practice of diagnosing a favoured linear instability and merely assuming that the turbulence arises from the same physical effect.

The basic situation in the edge of modern tokamak plasmas is that the region over which the parameters have 'edge values' (typical values of $\hat{\beta}$ and $\hat{\mu}$ both greater than unity [5]) is quite narrow in terms of the minor radius. The plasma is quite strongly inhomogeneous; the typical values as stated in equation (12) can be taken to obtain in rough terms only over a radial region comparable at most to $L_\perp$. In a homogeneous model computation, therefore, the radial domain

should not be set larger than this. In terms of ρ_s, the nominal size of 20π (about 64) is a reasonable compromise. The domain size in the y direction should be much larger in order to capture the physical anisotropy in the large scales represented by a typical minor radius of $a \sim 50$ cm; this is multiplied by $2\pi/q$ to obtain the typical distance in the y direction (perpendicular to the background magnetic field, within the flux surface) between the same field line between toroidal traverses. The physical aspect ratio for a circular tokamak edge is then $2\pi a/qL_\perp$, which is about 20 for the values we have chosen. One should increase the y/x domain aspect ratio until the results converge; a value of 4 can be considered to be safe [4]. In the s direction the principal consideration is global consistency: arbitrarily long parallel wavelengths would be chosen by the dynamics [28] but the combination of field line connection and periodicity [27] imposes a pseudo-periodic constraint (a phase shift of each y direction Fourier component) after one poloidal traversal along the magnetic field [53]. This feature must be preserved in a truncated flux tube computation in order to prevent the appearance of parallel wavelengths for each y direction Fourier component still kept in the computation [17]. The shifts between the coordinate systems on each grid node in the s direction (equation (8)) distribute these phase shifts among the s locations, such that the boundary condition is

$$f(x, y_{k+N}, s_{k+N}) = f(x, y_k, s_k) \tag{18}$$

(given N grid nodes in s), which looks periodic but is not, because the various nodes are on different coordinate systems [31]. The final consideration is that Dirichlet boundary conditions in x are most appropriate because if radial (x direction) flows appear they should be forced to turn around, due to the same considerations according to which the x domain is limited by $L_\perp$. The profiles of state variables with background gradients are maintained in boundary dissipation regions in the x direction, with only the $k_y = 0$ component affected in each case. Note that in the interior of the domain the dynamics of the profile is purely self-consistent (cf section 4 of [28]; in DALF3, only $\tilde{p}_e$ is so treated, with $\tilde{p}_i = \tau_i \tilde{p}_e$). The y direction is always periodic, because a displacement in y holding both x and s fixed is a toroidal displacement [17, 53]. The final consideration is that the grid resolution in both x and y should reach down to ρ_s (here, unity in normalized units); otherwise the action of the small scales on the rest of the dynamics as shown in section 4 is missed and one would wrongly conclude a general MHD-like character for the physics.

The basic toroidal case at nominal parameters is run on this grid as described in section 2, with the parameter set given in equation (11). In terms of conventional parameters, this corresponds to a collisionality of $\nu_* \approx 40$ (cf [18] for orientation), that is, high in those terms, but very moderate in the sense that $\nu_e \approx 3c_s/L_\perp$, and the mean free path is similar to qR. We also use both $\tau_i = 0$ and 1, i.e. both cold and warm ions. This is the DALF3 model, which we compare to the slab drift wave and toroidal resistive MHD models serving as the obvious control cases. The transition between a drift wave regime and a resistive ballooning regime as the parameter combination $C\omega_B$ is increased is being detailed elsewhere [52]; here, it is sufficient to compare the three cases at nominal parameters. We run them as we did the slab cases of figure 1, to $t = 1000$ allowing a well developed saturated state $500 < t < 1000$ over which all the diagnostics are averaged. The simplest comparison is the parallel structure of the disturbances, for which we strip out the $k_y = 0$ component, measure the square of the remaining part at each (x, y, s, t) and then average over x and y and over the saturated phase. We also measure the nonadiabatic part of the electron pressure in this fashion, given by

$$\tilde{h}_e \equiv \tilde{p}_e - \tilde{\phi}. \tag{19}$$

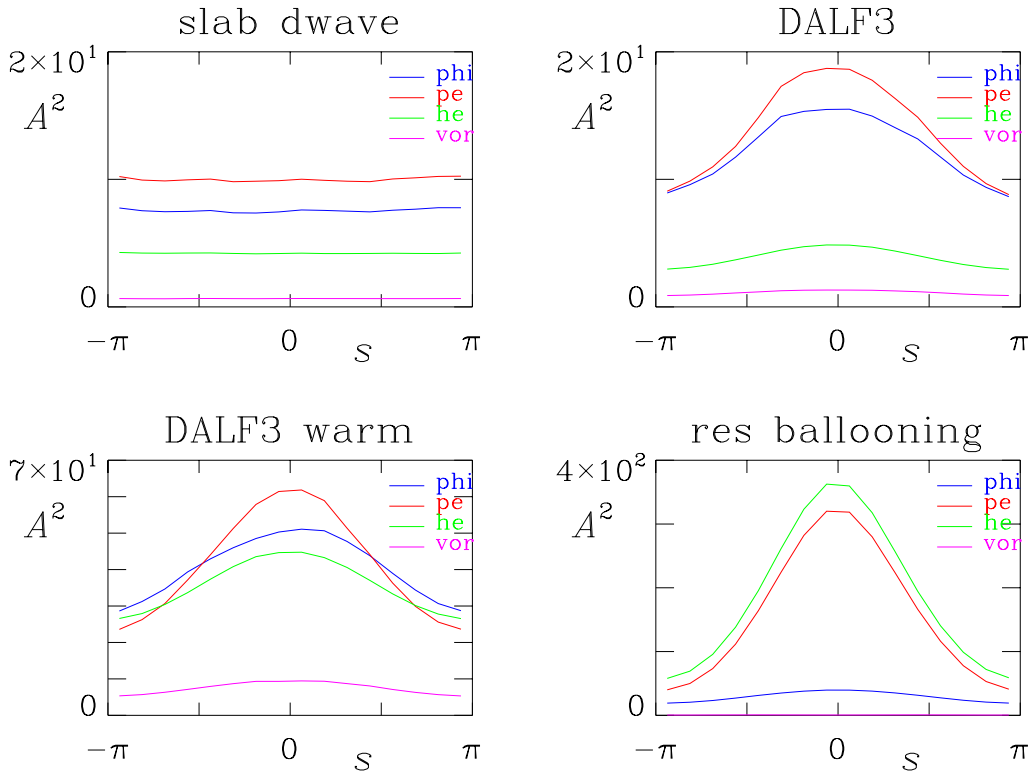

Figure 5. Squared amplitudes for $\tilde{\phi}$ (blue), $\tilde{p}_e$ (red), $\tilde{h}_e$ (green) and $\nabla_\perp^2\tilde{\phi}$ (pink) as a function of s for the slab, DALF3 with cold and warm ions, and resistive MHD models. Ballooning is severe in the MHD model but is present to a lesser extent in DALF3. The free energy dynamics, however, depends on the nonadiabatic part of the pressure disturbances, $\tilde{h}_e$, not the total $\tilde{p}_e$, and for DALF3 this is only weakly ballooned. The $\boldsymbol{E}\times\boldsymbol{B}$ turbulence is coupled to the Alfvén transients, ensuring importance of the nonadiabatic response. Warm ions enhance the interchange component to the DALF3 model but since $\tilde{h}_e < \tilde{p}_e$ it remains in the drift wave regime.

This is the force potential for $\tilde{J}_\parallel$ in Ohm's law (equation (2)) and it is also the only part of $\tilde{p}_e$ which yields a nonzero source term ($\omega_p\langle\tilde{p}_e v_E^x\rangle$ in equation (16)). Hence, the free energy dynamics responds to $\tilde{h}_e$ rather than $\tilde{\phi}$. This is an important consideration, because the result for the DALF3 model is that both $\tilde{p}_e$ and $\tilde{\phi}$ are ballooned towards $s = 0$, which is the outboard midplane of the torus. However, the key finding is that $\tilde{h}_e$ is only weakly ballooned, more like the slab model than the MHD model, for which $\tilde{h}_e \sim \tilde{p}_e > \tilde{\phi}$ even for this relatively high collisionality (we note here that the MHD model has violated its basic assumption, that ∇p of either species must be small compared to the static part of the electric field). By contrast, drift wave mode structure is characterized by $\tilde{p}_e \sim \tilde{\phi} > \tilde{h}_e$ even for robust nonadiabaticity, and this is where the DALF3 result landed.

There are two diagnostics that are particularly useful in discerning the qualitative nature of the coupling mechanism between $\tilde{\phi}$ and $\tilde{p}_e$. Drift wave turbulence is a strongly coupled system: the effective coupling constant through $\nabla_\parallel(\tilde{J}_\parallel/B)$ with $\nabla_\parallel\tilde{\phi}$ and $\nabla_\parallel\tilde{p}_e$ is of order unity or larger, and the electrons are more closely adiabatic than not, with the free energy dynamics coming

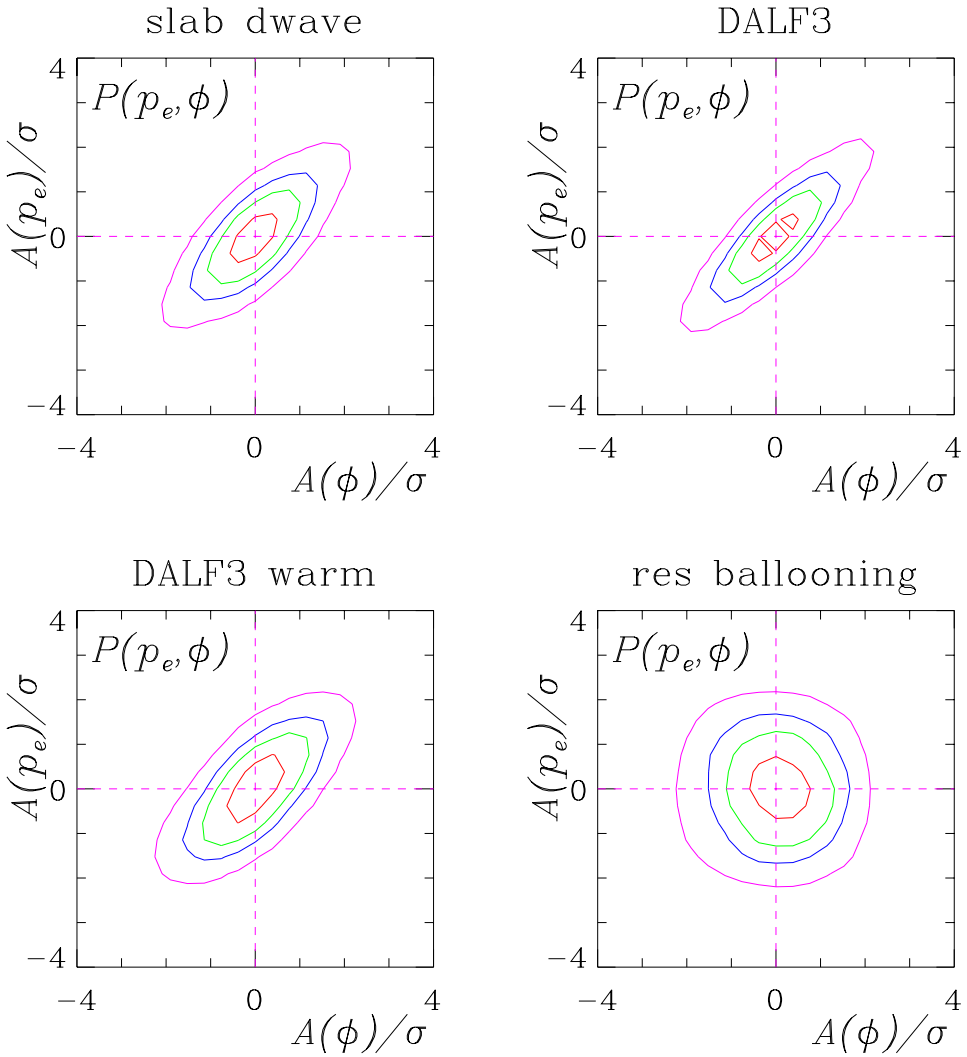

Figure 6. Cross correlation between $\tilde{p}_e$ and $\tilde{\phi}$ for the slab, DALF3 with cold and warm ions, and resistive MHD models. The strong correlation in the slab and DALF3 models reflects the adiabatic response (cf the smallness of $\tilde{h}_e$ in figure 5), while the neglect of $\tilde{p}_e \leftrightarrow \tilde{J}_\parallel$ coupling in the MHD model leaves the two state variables uncorrelated. The warm ions DALF3 case remains in the drift wave regime.

from the nonadiabaticity, the extent to which $\tilde{p}_e \neq \tilde{\phi}$ in the normalized state variables. Resistive ballooning (MHD) turbulence is, by contrast, a weakly coupled system: the coupling constant is ω_B which is rather small; the interchange forcing frequency given by $\omega_B(k_y\rho_s)$ is always smaller than the diamagnetic frequency given by $\omega_* = \omega_p(k_y\rho_s)$, and even the ideal interchange growth rate of $(\omega_B\omega_p)^{1/2}$ is smaller than ω_* since ω_B is smaller than the typical $k_y\rho_s$ values in the energy generating range of the spectrum. This leads to the two diagnostics of most use: the cross correlation between $\tilde{p}_e$ and $\tilde{\phi}$ and the PDF for the phase shift between these two state variables at each wavenumber k_y [4]. For the cross correlation $\tilde{p}_e$ and $\tilde{\phi}$ ($k_y \neq 0$ part) are sampled as a pair at $s = 0$ at each (x, y, t) in the saturated phase, each normalized to its own standard deviation,

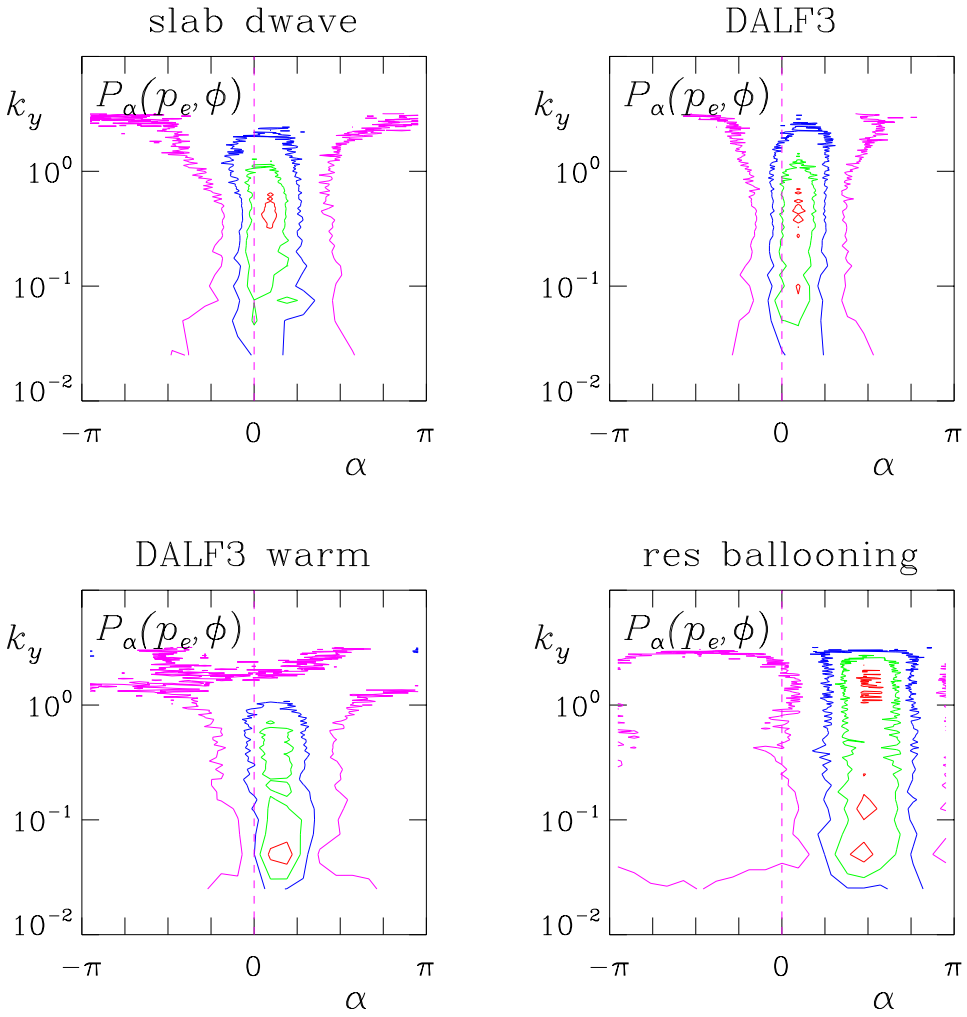

Figure 7. Probability distributions of the phase shift between $\tilde{p}_e$ and $\tilde{\phi}$ for the slab, DALF3 with cold and warm ions, and resistive MHD models. The phase shifts for the slab and DALF3 models reflect the adiabatic response (cf the smallness of $\tilde{h}_e$ in figure 5), while in the neglect of $\tilde{p}_e \leftrightarrow \tilde{J}_\parallel$ coupling in the MHD model the phase shifts are near the $\pi/2$ for which the gradient drive is maximum. The warm ions DALF3 case remains in the drift wave regime.

and binned on a 21×21 array over 4×4 standard deviations. The phase shifts

$$\alpha(k_y) \equiv \mathrm{Im}\log(\tilde{p}^*_{e k_y}\tilde{\phi}_{k_y}) \tag{20}$$

are found by Fourier decomposing $y \to k_y$ and then sampling at $s = 0$ at each x, k_y, t in the saturated phase, and then binned on an array of 21 over $-\pi < \alpha < \pi$ for each k_y. The cross correlations are shown in figure 6 and the phase shift distributions are shown in figure 7. The strong correlation between $\tilde{p}_e$ and $\tilde{\phi}$ and the relatively narrow phase shift distribution near a phase angle of zero is clear for the slab case, while a weak correlation and phase angles near $\pi/2$ is clear for the ballooning case. The DALF3 case clearly reflects the signature of the drift wave self-sustained turbulence rather than that of the ballooning case. This is consistent with the result for $\tilde{h}_e$ in figure 5 and reflects the fact that the strong coupling is the more important

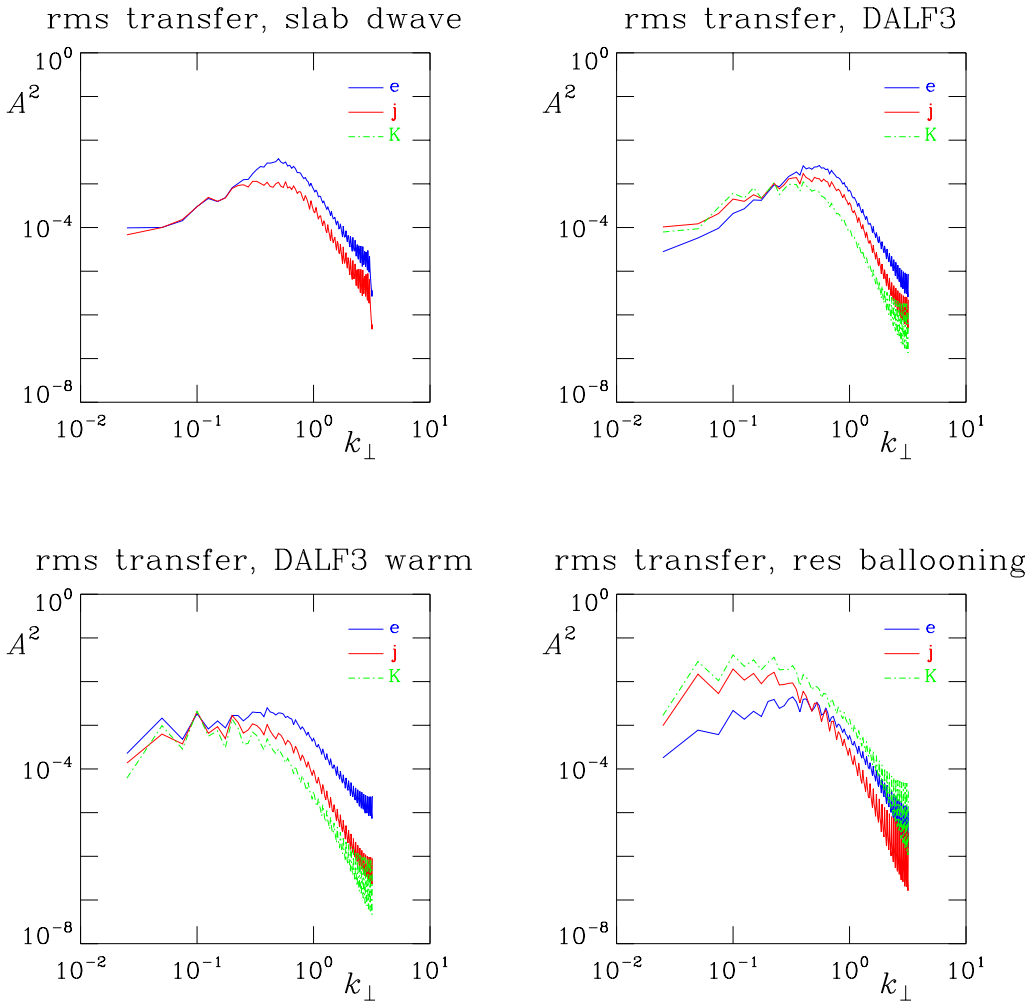

Figure 8. Rms energy transfer for the slab, DALF3 with cold and warm ions, and resistive MHD models, expressed as a 2D spectrum ($k_\perp$) representing the polarization, parallel and (for the toroidal cases) diamagnetic currents. The first two balance in the slab, while the last two balance in resistive MHD. The polarization current (vorticity nonlinearity) is subdominant for MHD because the dynamics is controlled by the linear ballooning instability. For DALF3, the nonlinear drift wave instability is more important and the diamagnetic current (interchange forcing) is subdominant. At higher collisionality or plasma beta, the larger scales become controlled by the interchange forcing, and the ballooning transition is realized when they decouple from the smaller scales. Warm ions enhance the interchange component to the DALF3 model but since $\tilde{h}_e < \tilde{p}_e$ it remains in the drift wave regime.

effect and hence that the adiabatic response is the more important energy transfer mechanism between the thermal gradient and the $\boldsymbol{E} \times \boldsymbol{B}$ eddies.

The vorticity dynamical spectra used to examine the nonlinear instability in section 4 are also useful. A version of this diagnostic which appears for the first time in this paper is the one which uses $k_\perp$ instead of k_y for the Fourier decomposition. Using a 2D Fourier decomposition,

the results are arranged in one-dimensional (1D) fashion with $k_\perp$ given by $k_\perp^2 = k_x^2 + k_y^2$. The same quantities as in figure 4 are shown in figure 8, again for the two control cases to which the complete DALF3 model is compared. The slab case balances the polarization and parallel currents [2], represented by the vorticity nonlinearity and the nonadiabaticity, respectively, with the linear $\partial/\partial t$ term small at low $k_\perp$. The MHD model balances the parallel and diamagnetic currents [54], the latter represented by the curvature operator, especially at long wavelength. The short wavelength vorticity nonlinearity is much weaker in the MHD model, indicating a synergy between polarization and parallel currents mediated by the adiabatic response; each makes the other larger. It is interesting to note the peak of this for $k_\perp \rho_s$ just below unity, reflecting the same importance of ρ_s scales we found in the electrostatic slab model. If the computations did not resolve ρ_s then this effect would have been missed. With the interchange forcing so dominant for low $k_\perp$, one would wrongly conclude that the turbulence is of the MHD type because this smaller scale vorticity dynamics would not be present to compete. Here again, the DALF3 result lands closer to drift wave mode structure, though both elements are clearly present. When the interchange forcing is strong enough to separate the larger from the smaller scales, the latter cease to be relevant and the turbulence passes into the ideal or resistive ballooning regime, if caused by $\hat{\beta}\omega_B$ or $C\omega_B$, respectively (cf [52]).

6. Temperature dynamics and the DALFTI model

We briefly also show some results from a model which retains all the complications of the electron and ion temperatures. Due to the low collisionality, the physics of Landau damping must be modelled to treat the parallel heat flux for each species. The basic scenario according to which this is done is the same as for the gyrofluid equations [5, 55]–[57], except that the parallel wavenumber $k_\parallel$ cannot be used as a parameter because $\nabla_\parallel$ is a nonlinear operator involving one of the dependent variables. The approximation used here is to retain the parallel heat flux as a dynamical variable as in the higher moment versions of the gyrofluid model, and introduce a damping operator on the heat flux given by a constant piece approximating $|k_\parallel|$ with $1/qR$ at the long wave side [4] and $k_\parallel^2$ with $(2\pi/16)(1/qR)^2$ at the short wave side, the latter replaced in practice by the use of a first-order upwind scheme for the temperature/heat flux dynamical subsystems [5]. Edge turbulence requires time-dependent Landau damping as well because not only is the mean free path comparable to qR but the timescale is also comparable to the collision frequency for electrons, and for ions the timescale is some two orders of magnitude faster. A dynamical equation for the heat flux captures the high frequency limit of the kinetic response function, even nonlinearly due to the use of the nonlinear $\boldsymbol{E} \times \boldsymbol{B}$ advective derivative [57], and it captures the weakly collisional regime as well by allowing for the appropriate time delay in the transmission of temperature information along field lines in what has been called the time-dependent thermal force [58]. In all, the electron and ion temperatures T_e and T_i become two additional state variables, and their parallel heat fluxes $q_{e\parallel}$ and $q_{i\parallel}$ enter as the corresponding flux variables, for a total of eight dependent variables, with background gradients and disturbances treated in the same fashion as for the DALF3 model. The equations are [29]

$$\frac{1}{B^2}\left[\frac{\mathrm{d}}{\mathrm{d}t}\nabla_\perp^2(\tilde{\phi}+\tilde{p}_i) + (\nabla \boldsymbol{v}_E) : (\nabla\nabla\tilde{p}_i)\right] = B\nabla_\parallel \frac{\tilde{J}_\parallel}{B} - \mathcal{K}(\tilde{p}_e + \tilde{p}_i) \tag{21}$$

$$\hat{\beta}\frac{\partial \tilde{A}_\parallel}{\partial t} + \hat{\mu}\frac{\mathrm{d}\tilde{J}_\parallel}{\mathrm{d}t} = \nabla_\parallel(p_e + \tilde{p}_e - \tilde{\phi}) - \hat{\mu}\nu_e\left[\eta\tilde{J}_\parallel + \frac{\alpha_e}{\kappa_e}(\tilde{q}_{e\parallel} + \alpha_e\tilde{J}_\parallel)\right] \tag{22}$$

$$\frac{\mathrm{d}}{\mathrm{d}t}(n_e+\tilde{n}_e) = B\nabla_\parallel \frac{\tilde{J}_\parallel - \tilde{u}_\parallel}{B} - \mathcal{K}(\tilde{p}_e - \tilde{\phi}) \tag{23}$$

$$\hat{\epsilon}\frac{\mathrm{d}\tilde{u}_\parallel}{\mathrm{d}t} = -\nabla_\parallel(p_e + p_i + \tilde{p}_e + \tilde{p}_i) + \mu_\parallel \nabla_\parallel^2 \tilde{u}_\parallel \tag{24}$$

$$\frac{3}{2}\frac{\mathrm{d}}{\mathrm{d}t}(T_e+\tilde{T}_e) = B\nabla_\parallel \frac{\tilde{J}_\parallel - \tilde{u}_\parallel - \tilde{q}_{e\parallel}}{B} - \mathcal{K}(\tilde{p}_e - \tilde{\phi}) - \frac{5}{2}\mathcal{K}(\tilde{T}_e) \tag{25}$$

$$\hat{\mu}\frac{\mathrm{d}\tilde{q}_{e\parallel}}{\mathrm{d}t} + a_{Le}(\tilde{q}_{e\parallel}) = -\frac{5}{2}\nabla_\parallel(T_e+\tilde{T}_e) - \frac{5/2}{\kappa_e}\hat{\mu}\nu_e(\tilde{q}_{e\parallel} + \alpha_e \tilde{J}_\parallel) \tag{26}$$

$$\frac{3}{2}\frac{\mathrm{d}}{\mathrm{d}t}(T_i+\tilde{T}_i) = B\nabla_\parallel \frac{\tau_i(\tilde{J}_\parallel - \tilde{u}_\parallel) - \tilde{q}_{i\parallel}}{B} - \tau_i\mathcal{K}(\tilde{p}_e - \tilde{\phi}) + \frac{5}{2}\tau_i\mathcal{K}(\tilde{T}_i) \tag{27}$$

$$\hat{\epsilon}\frac{\mathrm{d}\tilde{q}_{i\parallel}}{\mathrm{d}t} + a_{Li}(\tilde{q}_{i\parallel}) = -\frac{5}{2}\tau_i\nabla_\parallel(T_i+\tilde{T}_i) - \frac{5/2}{\kappa_i}\hat{\epsilon}\nu_i\tilde{q}_{i\parallel} \tag{28}$$

with current, pressures, and temperature ratio:

$$\tilde{J}_\parallel = -\nabla_\perp^2 \tilde{A}_\parallel \qquad \tilde{p}_e = \tilde{n}_e + \tilde{T}_e \qquad \tilde{p}_i = \tau_i\tilde{n}_e + \tilde{T}_i \qquad \tau_i = T_i/T_e \tag{29}$$

and Landau damping operators:

$$a_{Le} = \hat{\mu}^{1/2}(1 - 0.2\nabla_\parallel^2) \qquad a_{Li} = (\tau_i\hat{\epsilon})^{1/2}(1 - 0.2\nabla_\parallel^2) \tag{30}$$

including the three background gradients and their pressure combinations:

$$n_e = -\omega_n x \qquad T_e = -\omega_t x \qquad T_i = -\tau_i\omega_i x \qquad p_e = n_e + T_e \qquad p_i = \tau_i n_e + T_i. \tag{31}$$

The geometry and parameters are the same as already described for the DALF3 model in section 2 (avoid the possible confusion between the Braginskii ν_e and ν_i in the physical parameters and the normalized collision frequencies $\nu_{e,i} \leftarrow \nu_{e,i}L_\perp/c_s$). This is called the DALFTI model, extending drift Alfvén turbulence to the warm ion regime with Landau electrons and ions. The quasineutrality constraint (precisely equation (21)) is used to replace the divergence of the ion polarization and diamagnetic drifts with the electron parallel current and diamagnetic drift in equation (27). The combinations involving $(5/2)\mathcal{K}$ in the temperature equations result from the diamagnetic heat fluxes. The model for the collisional dissipation, given by the numerical constants

$$\eta = 0.51 \qquad \alpha_e = 0.71 \qquad \kappa_e = 3.2 \qquad \kappa_i = 3.9 \tag{32}$$

is chosen to recover the (pure hydrogen) Braginskii parallel heat fluxes and thermal forces in the short mean free path limits $\nu_e\hat{\mu}^{1/2} > 1$ and $\nu_i\hat{\epsilon}^{1/2} > 1$ and the low frequency limits $\nu_e > k_y\omega_n$ and $\nu_i > k_y\omega_n$ for electrons and ions, respectively, with $k_y\omega_n$ the normalized diamagnetic frequency for each wavenumber. For edge turbulence the limit $\nu_i > k_y\omega_n$ is never satisfied. The other three are usually marginal. Note that $C = 0.51\hat{\mu}\nu_e$.

A comparison to resistive MHD is somewhat problematic for this model, due to the diamagnetic contribution to the polarization drift and the fact that $\tilde{T}_i$ always exhibits interchange dynamics since it does not participate in the adiabatic response (it is the only state variable not present in equation (22)). It suffices, however, to set up a unit gradient case ($\omega_n = \omega_t = \omega_i = 1$) with unit temperature ratio ($\tau_i = 1$) and show the cross correlation and phase shift distributions for $\tilde{n}_e$ and $\tilde{\phi}$, in figure 9, for the same parameter combination as in equation (11), which for the individual collisionalities corresponds to $\nu_e = 3$ with $\nu_e = (2 \times 3670)^{1/2}\nu_i$. These exhibit a narrower range of dominant wavelengths, but comparison to the warm ions DALF3 case from figure 7 shows that the drift wave mode structure remains, represented by phase shifts below

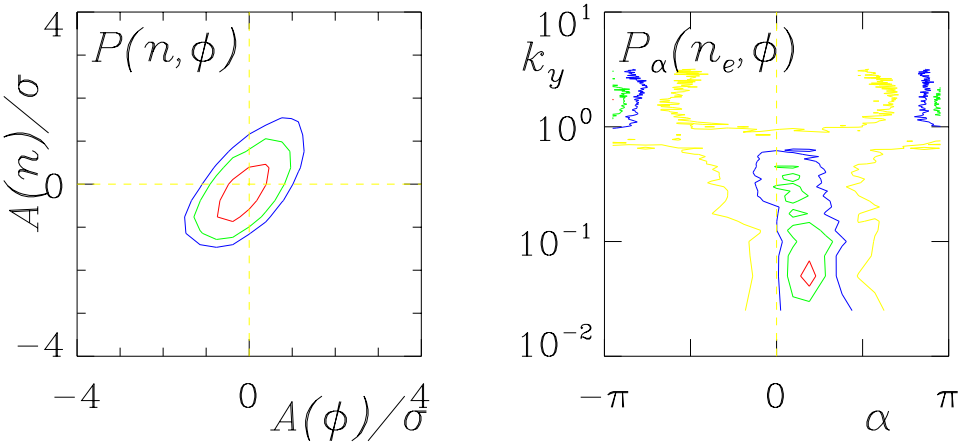

Figure 9. Cross correlation and phase shift distributions between $\tilde{n}_e$ and $\tilde{\phi}$ for the DALFTI model at nominal parameters. This reflects drift wave mode structure in the electron dynamics. For equal gradients ($\omega_n = \omega_t = \omega_i = 1$) the ion temperature disturbance $\tilde{T}_i$, does not have a special role although it does not participate in the $\tilde{J}_\parallel$ dynamics.

$\pi/4$ and strong cross correlation. The electron part of the system therefore follows drift wave dynamics, even though $\tilde{T}_i$ is fundamentally different. For equal gradients, $\tilde{T}_i$ is usually not dominant, though, and the dynamics is driven more by $\tilde{n}_e$ and $\tilde{T}_e$, and drift wave mode structure prevails.

Edge turbulence for these moderate parameters is usually either in this state or in one more reflective of toroidal ITG turbulence (cf [57], and also the review of turbulence models for the tokamak core in [59]). The canonical ITG case is adiabatic electrons (i.e. the extreme drift wave regime) with all the dynamics controlled by $\tilde{T}_i$ and ω_i, with a threshold in either R/L_T (that is, $2\omega_i/\omega_B$) or $\eta_i = L_n/L_{T_i}$ (that is, ω_i/ω_n). For edge turbulence ($\hat{\mu} > 1$; cf [4, 5]), the threshold disappears and we must use qualitative diagnosis to decide whether $\tilde{T}_i$ dominates. Fortunately we can discern this simply from the parallel envelope structure as in figure 5, which we show for some representative DALFTI cases in figure 10. All cases were at nominal parameters except where stated. The dynamics is of the drift wave type if the adiabatic response controls the electrons and the ion temperature does not have an especially dominant role. This is the case if all three of $\tilde{\phi}$, $\tilde{n}_e$ and $\tilde{T}_i$ are qualitatively similar, with the same spectrum and the same degree of ballooning (s dependence of the squared amplitude averaged over x and y), and if the overall heat fluxes $Q_e = (3/2)\langle \tilde{p}_e v_E^x \rangle$ and $Q_i = (3/2)\langle \tilde{p}_i v_E^y \rangle$ are approximately equal. This reflects $\tilde{\phi} \sim \tilde{p}_e \sim \tilde{p}_i$ due to the fact that $\tilde{T}_e < \tilde{n}_e$ usually, for $\eta_i \sim 1$. The turbulence is ITG-like if $\tilde{T}_i$ is dominant, with $\tilde{p}_i > \tilde{p}_e$ overall and $\tilde{T}_i$ larger and more strongly ballooned than any other state variable. ITG turbulence will also have $Q_i > Q_e$ even for $\tau_i = 1$. There is no sharp regime boundary, but a gradual transition roughly in the range $1 < \eta_i < 2$. Finally, the turbulence is ballooning-like if the special state variable is $\tilde{\phi}$, with that one now the largest and more strongly ballooned than any other (note this becomes the MHD regime, with $\nabla_\parallel \tilde{\phi} \gg \nabla_\parallel \tilde{p}_e$, hence $E_\parallel \approx 0$, and with $\nabla_\perp \tilde{\phi} \gg \nabla_\perp \tilde{p}_e$, hence $\boldsymbol{E}_\perp \gg \nabla_\perp \tilde{p}_e$). The transition to resistive ballooning (through ν_e) is gradual, with the transitional case at $\omega_B = C\omega_B \sim 1$. The transition to ideal ballooning (through $\hat{\beta}$) is sharper, occurring somewhat below $\alpha_M = \hat{\beta}\omega_B\omega_p \sim 1$, with $\omega_p = (\omega_n + \omega_t) + \tau_i(\omega_n + \omega_i)$

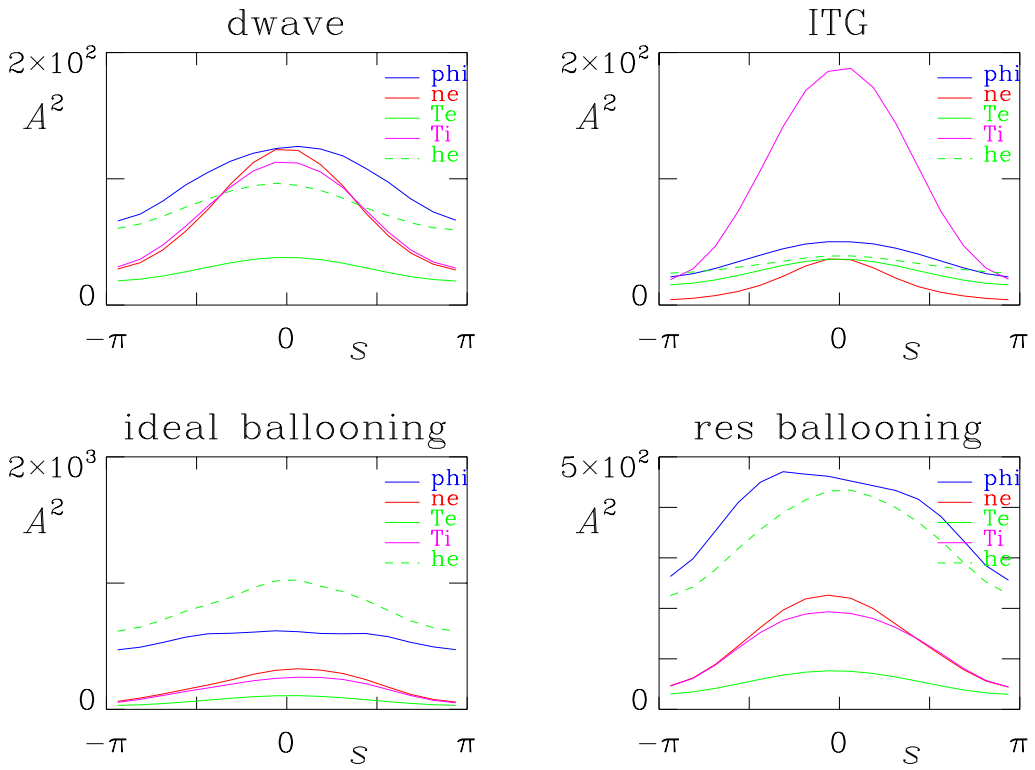

Figure 10. Squared amplitudes for $\tilde{\phi}$ (blue), $\tilde{n}_e$ (red), $\tilde{T}_e$ (green), $\tilde{T}_i$ (pink) and $\tilde{h}_e$ (green, broken) as a function of s for the DALFTI model exhibiting drift wave mode structure for equal gradients ($\omega_n = \omega_t = \omega_i = 1$), ITG mode structure for weaker $\omega_n = 0.5$, and ideal ballooning mode structure for $\hat{\beta} = 3$, and resistive ballooning mode structure for $\nu_e = 10$. Drift wave mode structure is $\tilde{h}_e < \tilde{n}_e$, reflecting the adiabatic response, and $\tilde{T}_i \sim \tilde{p}_e$, reflecting the lack of a special role for $\tilde{T}_i$. For ITG mode structure, $\tilde{T}_i$ is the largest and most strongly ballooned, but with the electron part of the system otherwise reflecting drift wave mode structure with $\tilde{\phi} \sim \tilde{p}_e$. Ballooning mode structure is $\tilde{\phi} \sim \tilde{h}_e > \tilde{p}_e \sim \tilde{T}_i$, reflecting the MHD regime for $\tilde{\phi}$, and Rayleigh–Taylor convection of both $\tilde{p}_e$ and $\tilde{p}_i$, the sole difference between the pressures being that $\tilde{T}_e$ is still weakly ballooned. In ideal ballooning, $\tilde{\phi}$ is sometimes weakly ballooned when significant shear Alfvén activity is also generated, as here.

giving the total pressure gradient (more detail is given in [52]). Both boundaries are pushed upward in realistic, finite aspect ratio tokamak geometry including all shaping effects (cf [5]), such that the typical regime of tokamak edge turbulence is somewhat below the ideal ballooning boundary and well below the resistive ballooning boundary.

As a final remark, we comment on the resulting transport scaling. The parameter range of interest in modern tokamak edges corresponds roughly to $1 < \nu_e < 3$ and $1 < \hat{\beta} < 5$, a relatively narrow domain set by all the various operational limits [18]. These numbers rest on the choice of $L_\perp$, obviously, the choice of which should reflect the average parametric state over the edge region which can be physically defined as $\hat{\mu} > 1$, the boundary at which the drift frequency and thermal transit frequency are equal (cf equation (10)). The radial distance between this point and

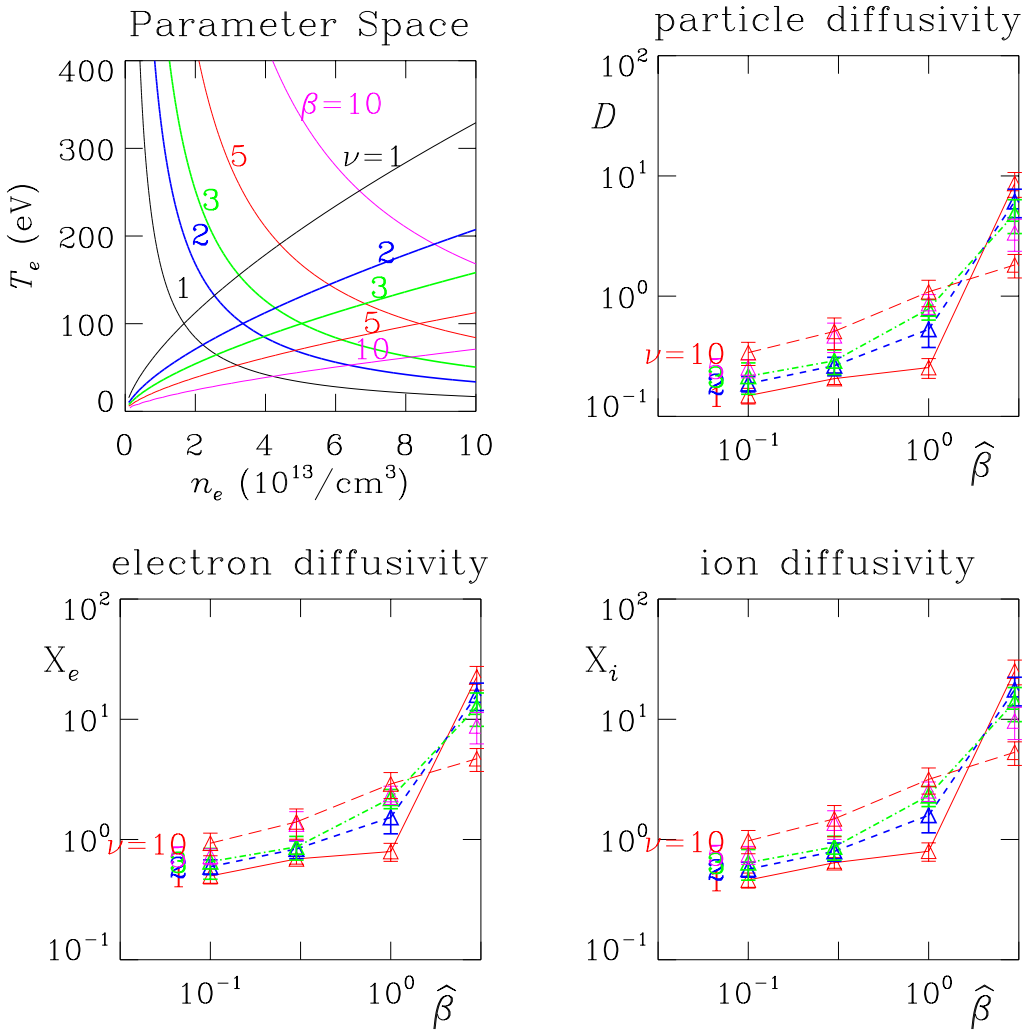

Figure 11. (Top left) Edge operation parameter regime, following the n_e and T_e space given in [18], showing the placement of cases with given $\hat{\beta}$ and ν_e, for otherwise nominal parameters (equation (11)). The other frames show the computed transport for the equal gradient cases, at the given $\hat{\beta}$ and ν_e values (for which $C = 2.55\nu_e$). The vertical axes give the corresponding diffusivities in units of $\mathrm{m}^2\ \mathrm{s}^{-1}$. The electron and ion diffusivities are totals, $X_{e,i} = \chi_{e,i} + (3/2)D$.

the last closed flux surface for a representative case can be taken for $L_\perp$ as a standard definition, for which we have set $L_\perp = 4.25$ cm. This also sets $\hat{\mu} = 5$. We vary $\hat{\beta}$ and ν over the range shown in figure 11, and for unit gradients we find the scaling as shown. Varying the parameters in this fashion varies n_e and T_e at constant B, not at constant $\rho_s/L_\perp$, a difference which must be taken into account when presenting the scaling, as seen in figure 11. In equal-gradient cases the turbulent heat fluxes of electrons and ions are comparable, and both conductive heat diffusivities are about 1.5 times the particle diffusivity. In physical units, the particle diffusivity, D, is the particle flux, $F_n = \langle \tilde{n}_e v_E^x \rangle$ divided by $|\nabla n_e|$. The heat fluxes $Q_{e,i}$ are given by both conductive, $(3/2)n_e \langle \tilde{T}_{e,i} v_E^x \rangle$, and convective, $(3/2)T_{e,i} \times F_n$, parts. The thermal diffusivities, $\chi_{e,i}$, are the

conductive heat fluxes divided by $n_e|\nabla T_{e,i}|$. The scaling versus collisionality is very similar to results in the simple sheared slab, approximately $\chi_{e,i} \propto C\chi_{GB}$, with $\chi_{GB} = c_s\rho_s^2/L_\perp$ the standard gyro-Bohm diffusivity (recall $C = 0.51\hat{\mu}\nu_e$).

We note that there is no indication of a transport regime break except for the sharp rise with $\hat{\beta}$ which reflects the onset of ideal ballooning. Although the results are very consistent with L-mode transport, we cannot explain the transition to the H-mode [60] with these results. The same conclusion results using the most detailed model in the flux surface geometry of an actual Grad–Shafranov equilibrium having the same ellipticity and aspect ratio of modern tokamaks [5]. The transition is associated with the development of a strong radial derivative of the radial electric field profile, which corresponds to an $\boldsymbol{E} \times \boldsymbol{B}$ vorticity layer and hence an $\boldsymbol{E} \times \boldsymbol{B}$ velocity shear layer [61]. The turbulence is often invoked as a self-consistent generator of this shear layer [62]. Although zonal flows [63] do play a part in these turbulence computations, we find a certain resilience to the generation of long-lived mean flows that could account for the transition [64]; recent investigations have found that the geodesic curvature ($\mathcal{K}^x$) transfers free energy out of the zonal flows back into the turbulence [65]. Recent work in edge modelling suggests possibilities for the shear layer's development as part of the neoclassical equilibrium as a function of parameters [66, 67]. As continual maintenance is required to support a mean flow against the turbulence in this geometry, the actual L-to-H transition probably comes from one of these possibilities rather than directly from the turbulence. Attempts to model this self-consistently, not by manual insertion of a profile pedestal but by means of an artificial heating function, are ongoing.

7. Conclusions

Self-sustained drift wave turbulence is a hallmark example of nonlinearity and nonlinear instability in plasma physics. Linear drift waves by themselves are either stable or very weakly unstable, but the existence of the nonlinear $\boldsymbol{E} \times \boldsymbol{B}$ terms involving $\boldsymbol{E} \times \boldsymbol{B}$ vorticity and pressure fluctuations leads to greatly enhanced activity in the dynamics of the parallel current (i.e. nonadiabatic passing electrons), leading to drastic changes in the morphology of the turbulence and its mode structure, not only due to the differing spectral transfer tendencies of the two main nonlinearities but also the ability of the nonlinearities to oppose the divergence of the parallel current [2, 6]–[8]. This was found to lead to a form of nonlinear instability called self-sustained turbulence in the simple 2D sheared slab model [7], in which the linear eigenmodes are all stable [20]. New computational studies at very high resolution have been presented herein, demonstrating the initial amplitude threshold and detailing several of the properties the nonlinearities introduce, thereby placing the nonlinear instability on this same secure footing in 3D. Both of the principal nonlinearities are at work: the vorticity one, $\boldsymbol{v}_E \cdot \nabla\nabla_\perp^2\tilde{\phi}$, scatters drift energy among the available degrees of freedom with little sub-grid dissipation, supporting the parallel currents and thereby catalyzing the turbulence; and the pressure one, $\boldsymbol{v}_E \cdot \nabla\tilde{p}_e$, acts as a more familiar diffusive mixing, providing most of the sub-grid dissipation and hence the saturation mechanism.

Having established the nonlinear instability, the turbulence resulting from a case at typical tokamak edge parameters in a globally consistent tokamak flux tube geometry [31] was compared to two control cases at the same parameters representing the sheared slab and resistive MHD ballooning models. This was done not by looking subjectively at the morphology but by examining the mode structure underlying the mechanisms of free energy transfer between the

principal state variables, $\tilde{p}_e$ and $\tilde{\phi}$. The most useful of these diagnostics are the cross correlation and phase shift probability distributions between the two state variables. Spectra of the transfer terms in the vorticity equation were also found useful. Together, these show that the tendency of interchange forcing effects to try to balance the parallel and diamagnetic currents [54] is overcome by the nonlinear balance between polarization and parallel currents which characterize drift wave mode structure. When the interchange forcing does take over, clear regime breaks occur, with the relevant one being the onset of ideal ballooning which appears to set the plasma beta (pressure gradient) limit seen in experiments [18]. In the operationally stable part of parameter space, the saturated level of the turbulence and the resulting averaged thermal energy transport are controlled principally by the nonlinear mechanisms underlying self-sustained drift wave turbulence, even in the presence of the linear ballooning-type instabilities introduced by the toroidicity.

Typical cases contrasting the signatures of drift wave, ITG mode and ballooning mode turbulence were also presented. If electrostatic potential fluctuations were more available to experimental analysts, the contrasting signatures developed herein would be very useful in determining the nature of tokamak edge turbulence experimentally. Indeed, most existing Langmuir probe information shows fluctuations in the two state variables at similar amplitude, which is the case in either ITG or drift wave turbulence. Ion temperature fluctuation data would, however, be needed to tell these latter two apart. The transport scalings versus plasma beta and collisionality, together with sheared $\boldsymbol{E} \times \boldsymbol{B}$ flow analysis which appears mostly elsewhere [5, 64, 65], shows that the turbulence does not by itself account for the long-lived $\boldsymbol{E} \times \boldsymbol{B}$ shear layer experimentally associated with the L-to-H confinement transition [60, 61]. This indicates the need for mechanisms associated with the neoclassical equilibrium [66, 67], which could maintain the $\boldsymbol{E} \times \boldsymbol{B}$ shear layer in a way external to the turbulence.

Appendix. Linear, quasilinear and nonlinear effects in the turbulence

Spatio-temporal morphology of the turbulence (two- or three-dimensional contour plots or animations thereof) is not very helpful by itself in discerning the physical mechanisms which underly the turbulence and the transport it causes, but it can do well to illustrate certain features once these have been determined by other means. An illustration of the meaning of nonlinearity to turbulence is one such case. One often sees references to linear or nonlinear dynamics, or quasilinear modelling of the transport linear instabilities might cause (cf, e.g., [46]). An animation of the spatial form of the state variable doing the transporting ($\tilde{\phi}$) and the transported quantity ($\tilde{p}_e$) is given in the associated multimedia enhancements page, with which these three concepts can be elucidated. This is a DALF3 case with nominal parameters run to very late times to obtain long term energetics statistics. The colour frames show the distribution of $\tilde{\phi}$ and $\tilde{p}_e$ in the drift plane (xy). Only part of the computational domain is shown; the entire domain is set up as noted in section 5. The $\boldsymbol{E} \times \boldsymbol{B}$ velocity can be inferred using $\tilde{\phi}$ as the stream function—clockwise around a maximum (red) and counterclockwise around a minimum (blue). One finds turbulent $\boldsymbol{E} \times \boldsymbol{B}$ flow eddies, which cause and move disturbances in the electron pressure ($\tilde{p}_e$). A flow through a pressure disturbance can be inferred from the phase shift—given $\tilde{\phi}$ and $\tilde{p}_e$ of the same sign (red, positive; blue, negative), the phase shift is positive if the $\tilde{\phi}$ is slightly displaced towards positive y (upward). Local transport events are seen, as not only do flows go through $\tilde{p}_e$-maxima down the gradient (rightward), but the flows also move the pressure disturbances in an ordered way as well as in a more random sense which leads to their shearing apart. The flows also transport their own vorticity (through $\boldsymbol{v}_E \cdot \nabla \nabla_\perp^2 \tilde{\phi}$) and hence shear themselves apart as well.

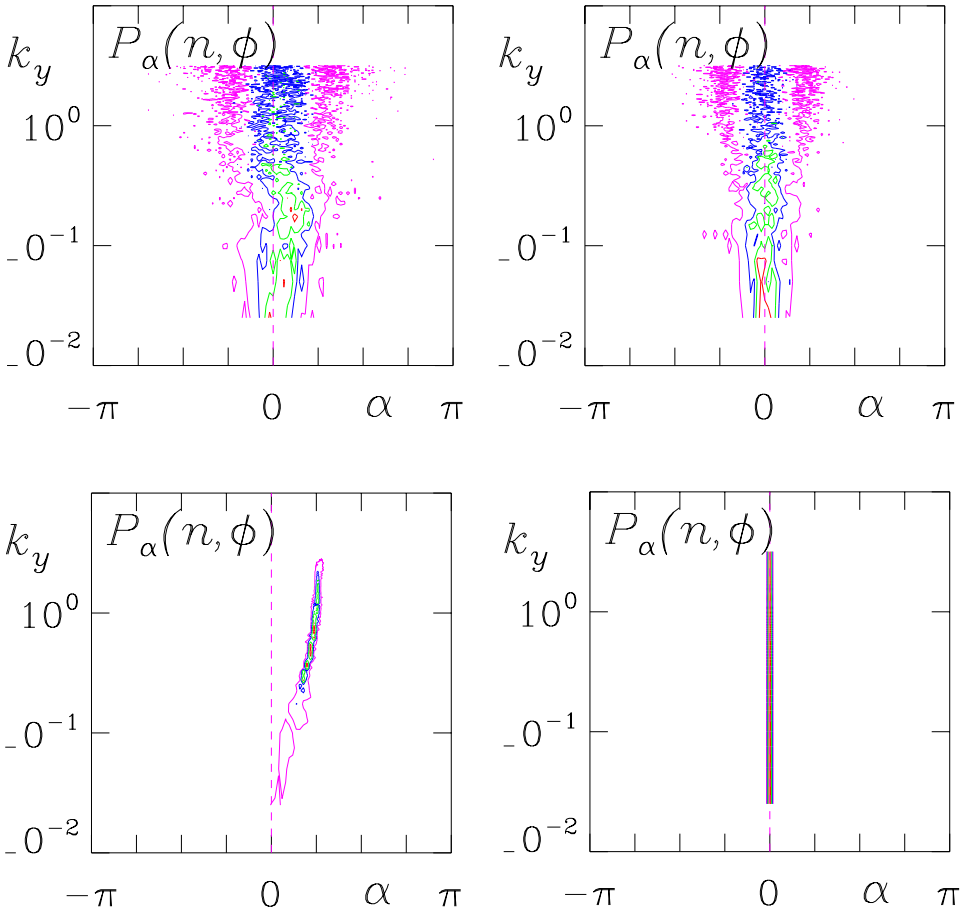

Figure A.1. The nonlinear instability mechanism, displayed in the simple 2D Wakatani–Hasegawa model with n and ϕ as the variables [2, 8]. The two cases on the bottom row are linear; the two above are nonlinear. The two on the left are with all terms present; the two on the right are with the gradient drive term absent. The linear case with no forcing at bottom right shows an adiabatic electron response, with the phase shift always at zero. The nonlinearities act to broaden the phase shift distribution around zero, but with both positive and negative values possible, as seen at upper right. With the gradient drive present the linear case at lower left shows a spectrum of instabilities, each with a definite phase shift. The corresponding nonlinear case at upper left shows the same broadened phase shift distribution as without the gradient drive, but with the entire distribution shifted to positive values. Comparison of the phase shifts in the two cases with the gradient present (upper and lower left) shows that the stronger linear instabilities near $k_y\rho_s = 1$ are wiped out by the turbulence. A linear instability with a strong growth rate would have to be present at low k_y to alter this turbulent state.

At certain times, one sees a particularly isolated flow eddy and at the same time strong growth of a pressure disturbance in place at the same location, slightly shifted towards positive y from the eddy if the signs of $\tilde{\phi}$ and $\tilde{p}_e$ are positive. This represents linear excitation and growth of a disturbance in the presence of its gradient ($\boldsymbol{v}_E \cdot \nabla p_e \rightarrow -\omega_p \partial\tilde{\phi}/\partial y$). The disturbance is created at the same scale (k_y) that the flow has. The flow also strengthens in turn, due to the

linear instability, which this case is caused by interchange forcing.

The flow initially stops growing when the pressure disturbance depletes the local gradient. This is what is meant by quasilinear flattening—$\tilde{p}_e$ has appeared with a large enough gradient to cancel out the background ∇p_e. At about the same time, the disturbance itself begins to move in the direction of the flow. This is the onset of nonlinearity, in this case the pressure one ($\boldsymbol{v}_E \cdot \nabla \tilde{p}_e$). Then the flow begins to turn around as it begins to shear itself apart ($\boldsymbol{v}_E \cdot \nabla \nabla_\perp^2 \tilde{\phi}$) and at the same time mix the disturbance ($\boldsymbol{v}_E \cdot \nabla \tilde{p}_e$), first into thin sheets and then into small 'droplets' which lose their identity in the turbulent mix. When the flows and pressure disturbances are actually turbulent, the mode structure acquires drift wave character, as diagnosed in section 5. Short-lived zonal flows also appear as bursty displacements of a whole line of eddies and disturbances up or down in the y direction. This is also visible as a vertical stripe in the pattern of $\tilde{\phi}$ which is short-lived. A long-lived mean flow would represent the coherent shearing of the entire drift plane, but no such case is observed.

The contrast between these concepts is clear: linear interactions proceed between disturbances at the same scale. Linear instability represents mutual growth of two or more quantities at the same scale. Quasilinear interactions are those by which a linear interaction affects the background. The three-wave interaction is between mode $\boldsymbol{k}_\perp$, mode $-\boldsymbol{k}_\perp$ and mode zero; the wave is essentially beating against itself. Nonlinear interactions are those by which several disturbances at differing scales interact with each other. Each does have its own quasilinear interaction with the background, but there are more three-wave triads with nonzero wavenumber, and these usually dominate. When there are many of these triads, that is, many degrees of freedom, the interactions are statistically incoherent and turbulence results. One sees this in the short-lived nature of any of the spatial structures, that is, a short correlation time (comparable to or shorter than the growth time of any linear instability) is a general property of turbulence. It is important to note that the linear interactions may still produce strong cross correlation between two variables, even though the various wavenumbers remain weakly correlated or completely uncorrelated. But to establish the presence or absence of cross correlation, we require the appropriate diagnostic to measure the degree of correlation.

One other important thing cannot be discerned from these animations: the extent to which nonlinearities cause effective dissipation by random mixing. Is the nonlinearity more like diffusive mixing or incoherent scattering? And does a nonlinearity jump in to assume the role of excitation away from the linear instability (as shown in figure A.1)? To answer questions such as these we require the sort of investigations presented in the body of this paper. We cannot learn their answers by looking at transport scalings or contour animations. Ultimately, one cannot learn the physics underlying the turbulence from such superficial information, or even from the well-studied character of a set of linear instabilities. One must perform the statistical diagnosis in the context of the fully developed turbulence itself, and ultimately one must look at the statistics of two or more variables in concert, not just the statistical behaviour of just one of them.

References

[1] Mikhailovskii A B 1974 *Theory of Plasma Instabilities* vol 2 (New York: Consultants Bureau) p 87
[2] Wakatani M and Hasegawa A 1984 *Phys. Fluids* **27** 611
[3] Mikhailovskii A B and Rudakov L I 1963 *Sov. Phys.–JETP* **17** 621
See also Tang J T and Luhmann N C Jr 1976 *Phys. Fluids* **19** 1935 for a very clear exposition
[4] Scott B 1997 *Plasma Phys. Control. Fusion* **39** 1635

[5] Scott B 2000 *Phys. Plasmas* **7** 1845
[6] Scott B, Biglari H, Terry P W and Diamond P H 1991 *Phys. Fluids* B **3** 51
[7] Scott B 1990 *Phys. Rev. Lett.* **65** 3289
Scott B 1992 *Phys. Fluids* B **4** 2468
[8] Camargo S, Biskamp D and Scott B 1995 *Phys. Plasmas* **2** 48
[9] Rowan W L, Klepper C C, Ritz Ch P, Bengston R D, Gentle K W, Phillips P E, Rhodes T L, Richards B and Wootton A J 1987 *Nucl. Fusion* **27** 1105
[10] Ritz Ch P, Brower D L, Rhodes T L, Bengston R D, Levinson S J, Luhmann N C Jr, Peebles W A and Powers E J 1987 *Nucl. Fusion* **27** 1125
[11] Ritz Ch P, Powers E J and Bengston R D 1989 *Phys. Fluids* B **1** 153
[12] Ritz Ch P, Bravanec R V, Schoch P M, Bengston R D, Boedo J A, Forster J C, Gentle K W, He Y, Hickok R L, Kim Y J, Lin H, Phillips P E, Rhodes T L, Rowan W L, Valanju P M and Wootton A J 1989 *Phys. Rev. Lett.* **62** 1844
[13] Rhodes T L, Ritz Ch P and Bengston R D 1993 *Nucl. Fusion* **33** 1147
[14] Filippas A V, Bengston R D, Li G-X, Meier M, Ritz Ch P and Powers E J 1995 *Phys. Plasmas* **2** 839
[15] Endler M, Niedermeyer H, Giannone L, Holzhauer E, Rudyj A, Theimer G, Tsois N and ASDEX Team 1995 *Nucl. Fusion* **35** 1307
[16] Hidalgo C 1995 *Plasma Phys. Control. Fusion* **37** A53
[17] Scott B 1998 *Phys. Plasmas* **5** 2334
[18] Suttrop W *et al* 1997 *Plasma Phys. Control. Fusion* **39** 2051
[19] Molvig K, Hirshman S P and Whitson J C 1979 *Phys. Rev. Lett.* **43** 582
[20] Ross D W and Mahajan S M 1978 *Phys. Rev. Lett.* **40** 324
Tsang K T, Catto P J, Whitson J C and Smith J 1978 *Phys. Rev. Lett.* **40** 327
[21] Wootton A J, Carreras B A, Matsumoto H, McGuire K, Peebles W A, Ritz Ch P, Terry P W and Zweben S J 1990 *Phys. Fluids* B **2** 2879
[22] Terry P W and Horton C W Jr 1982 *Phys. Fluids* **25** 491
[23] Scott B 1992 *Plasma Phys. Control. Fusion* **34** 1977
[24] Freidberg J P 1987 *Ideal Magnetohydrodynamics* (New York: Plenum) p 267
[25] Chandrasekhar S 1961 *Hydrodynamic and Hydromagnetic Stability* (Oxford: Clarendon) ch 10
[26] Coppi B 1977 *Phys. Rev. Lett.* **39** 939
See also Freidberg *Phys. Rev. Lett.* **39** 268
[27] Connor J W, Hastie R J and Taylor J B 1978 *Phys. Rev. Lett.* **40** 396
[28] Scott B 1997 *Plasma Phys. Control. Fusion* **39** 471
[29] Scott B 1998 *Contrib. Plasma Phys.* **38** 171
[30] Hinton F L and Horton C W Jr 1971 *Phys. Fluids* **14** 116
[31] Scott B 2001 *Phys. Plasmas* **8** 447
[32] Braginskii S I 1965 *Rev. Plasma Phys.* **1** 205
[33] Van Leer B 1979 *J. Comput. Phys.* **32** 101
[34] Colella P 1990 *J. Comput. Phys.* **87** 171
[35] Hasegawa A and Mima K 1977 *Phys. Rev. Lett.* **39** 205
Hasegawa A and Mima K 1978 *Phys. Fluids* **21** 87
[36] Kraichnan R H 1967 *Phys. Fluids* **10** 1417
[37] Weiland J 2000 *Collective Modes in Inhomogeneous Plasma: Kinetic and Advanced Fluid Theory (IOP Plasma Physics Series)* (Bristol: Institute of Physics)
[38] Gang F-Y, Scott B and Diamond P H 1989 *Phys. Fluids* B **1** 1331
[39] Rogister A and Hasselberg G 1982 *Phys. Rev. Lett.* **48** 249
[40] Gang F-Y, Diamond P H and Rosenbluth M N 1991 *Phys. Fluids* B **3** 68
[41] Cheng C Z and Okuda H 1978 *Phys. Rev. Lett.* **41** 1116
[42] Biskamp D and Zeiler A 1995 *Phys. Rev. Lett.* **74** 706

[43] Bell J B, Colella P and Glaz H M 1989 *J. Comput. Phys.* **85** 257
Bell J B and Marcus D L 1992 *J. Comput. Phys.* **101** 334
[44] Grauer R and Marliani C 1995 *Phys. Plasmas* **2** 41
[45] Colella P and Puckett E G 1994 *Modern Numerical Methods for Fluid Flow (Lecture Notes)* Department of Mechanical Engineering (Berkeley, CA: University of California Press) ftp://watt.berkeley.edu/e266/
[46] Liewer P C 1985 *Nucl. Fusion* **25** 543
[47] Shafranov V D and Yurchenko E I 1968 *Nucl. Fusion* **8** 329
See also [27]
[48] Ware A S, Diamond P H, Biglari H, Carreras B A, Charlton L A, Leboeuf J-N and Wootton A J 1992 *Phys. Fluids* B **4** 877
[49] Ross D W 1994 *Phys. Plasmas* **1** 2630
[50] Scott B 1995 *Plasma Physics and Controlled Nuclear Fusion Research 1994 (IAEA, Vienna 1995)* vol 3, p 447
[51] Scott B 1993 *Plasma Physics and Controlled Nuclear Fusion Research 1992 (IAEA, Vienna 1993)* vol 2, p 203
[52] Scott B 2002 Drift wave versus interchange turbulence in toroidal flux tube geometry: linear versus nonlinear mode structure *Phys. Plasmas* submitted
[53] Dewar R L and Glasser A H 1983 *Phys. Fluids* **26** 3038
[54] Guzdar P N, Drake J F, McCarthy D, Hassam A B and Liu C S 1993 *Phys. Fluids* B **5** 3712
[55] Hammet G and Perkins F W 1990 *Phys. Rev. Lett.* **64** 3019
[56] Dorland W and Hammett G 1993 *Phys. Fluids* B **5** 812
[57] Beer M A and Hammett G W 1996 *Phys. Plasmas* **3** 4046
[58] Hassam A B 1980 *Phys. Fluids* **23** 38
[59] Dimits A M, Bateman G, Beer M A, Cohen B I, Dorland W, Hammett G W, Kim C, Kinsey J E, Kotschenreuther M, Kritz A H, Lao L L, Mandrekas J, Nevins W M, Parker S E, Redd A J, Shumaker D E, Sydora R and Weiland J 2000 *Phys. Plasmas* **7** 969
[60] Wagner F *et al* 1982 *Phys. Rev. Lett.* **49** 1408
[61] Detailed pedestal profile measurements from D-III-D: Gohil P, Burrell K H, Doyle E J, Groebner R J, Kim J and Seraydarian R P 1994 *Nucl. Fusion* **34** 1057
[62] Diamond P H and Kim Y B 1991 *Phys. Fluids* B **3** 1626
[63] Lin Z, Hahm T S, Lee W W, Tang W M and White R B 1998 *Science* **281** 1835
[64] Scott B 2000 *Physics of Zonal Flows in Drift Wave Turbulence Theory of Fusion Plasmas* ed J Connor, O Sauter and E Sindoni (Bologna: Editrice Compositori) pp 413–18
[65] Scott B 2002 Zonal flows and electromagnetic drift wave turbulence *Phys. Lett.* A submitted
[66] Heikkinen J A, Kiviniemi T P and Peeters A G 2000 *Phys. Rev. Lett.* **84** 487
[67] Morozov D, Rozhansky V, Herrera J and Soboleva T 2000 *Phys. Plasmas* **7** 1184